# Residual Properties of Ultra-High Performance Concrete Containing Steel-polypropylene Hybrid Fiber Exposed to Elevated Temperature at Early Age

Tan Wang[a], Min Yu[a]*, Jie Tian[a], Zewen Sun[a], Chunlei Yu[a], Jianqiao Ye[b]

[a] School of Civil Engineering, Wuhan University, Wuhan 430072, China;

[b] School of Engineering, Lancaster University, Lancaster LA1 4YR, UK

**Abstract:** To investigate residual properties of Ultra-High Performance Concrete (UHPC) containing steel-polypropylene hybrid fiber subjected to fire accidents during construction, uniaxial compressive tests were carried out on UHPC exposed to elevated temperature at early age. The test parameters include the age exposed to elevated temperature, temperature levels, steel fiber content and coarse aggregate content. Based on the test results, failure mode, strength, elastic modulus, peak strain, and strain-stress response of the tested specimens were analysed. Additionally, microstructures of the specimens were characterized using X-ray diffraction and scanning electron microscopy. The test results show that up to 600°C, the residual compressive strength of the UHPC generally increases with age due to the improved resistance and accelerated hydration. At 800°C, the strength decreases slightly with age due to the porosity and carbonation reactions. Finally, an empirical formula was proposed to predict the compressive strength, peak strain, elastic modulus, and the uniaxial compressive stress-strain constitutive model of the UHPC exposed to elevated temperature at early age.

**Keywords：** Ultra-High Performance Concrete; Steel-polypropylene hybrid fiber; Early age; Elevated temperatures; Residual performance.

## Notations

| | |
|---|---|
| $f_c$, $E$, $\varepsilon_p$ | The cylinder strength, elastic module and peak strain of matured UHPC at room temperature (20℃, 56d) , respectively. |
| $f^a_{c,T,t_T}$, $E^a_{T,t_T}$, $\varepsilon^a_{p,T,t_T}$ | The cylinder strength, elastic module and peak strain of UHPC exposed to elevated temperature at early age, respectively. |
| $f_{c0}$, $E_0$, $\varepsilon_{p0}$ | The cylinder strength, elastic module and peak strain of matured mortar at room temperature (20℃, 56d) , respectively. |
| $k^a_{c,T,t_T}$, $k^a_{E,T,t_T}$, $k^a_{\varepsilon,T,t_T}$ | Modified parameter considering the fire-damaged age of cylinder strength, elastic module and peak strain, respectively. |
| $k_{c,ca}$, $k_{E,ca}$, $k_{\varepsilon,ca}$ | Modified parameter considering the volume fraction of coarse aggregate of cylinder strength, elastic module and peak strain, respectively. |
| $k_{c,sf}$, $k_{E.sf}$, $k_{\varepsilon,sf}$ | Modified parameter considering the volume fraction of steel fiber of cylinder strength, elastic module and peak strain, respectively. |
| $k^a_{c,T}$, $k^a_{E,T}$, $k^a_{\varepsilon,T}$ | Modified parameter considering temperature of cylinder strength, elastic module and peak strain, respectively. |
| $k^a_{c,t_T}$, $k^a_{E,t_T}$, $k^a_{\varepsilon,t_T}$ | Modified parameter considering early-age of cylinder strength, elastic module and peak strain, respectively. |
| $T$, $t_T$ | Temperature and the age exposed to elevated temperature, respectively. |
| $V_{ca}$, $V_{sf}$ | The volume fraction of coarse aggregate and steel fiber, respectively. |

# 1 Introduction

Post-fire assessments are critical for ensuring safety and longevity of building structures, given the frequent occurrence of fire incidents. Fire exposure leads to thermal degradation, causing a structure to lose its original properties. Continuing to use these compromised structures poses significant safety risks, while demolishing them prematurely results in resource wastage. Therefore, accurately assessing residual mechanical properties of a post-fire structure is imperative to mitigate safety risks, prevent unnecessary demolition, and reduce resource wastage. Additionally, statistical studies [1] have indicated that there has been an increase in the number of fire incidents occurring when a structure is under construction (Figure 1), many of which have been reported in the medium[2-4]. As shown in Figure 2, concrete in its early age during construction is particularly susceptible to fire damage, which subsequently impacts its performance

in service.

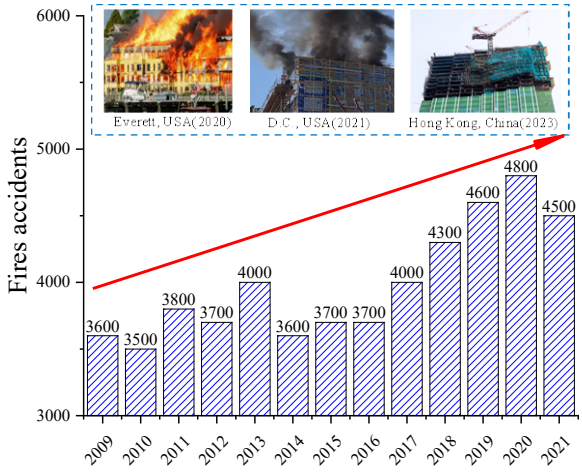


Figure 1 Fire accident number during construction

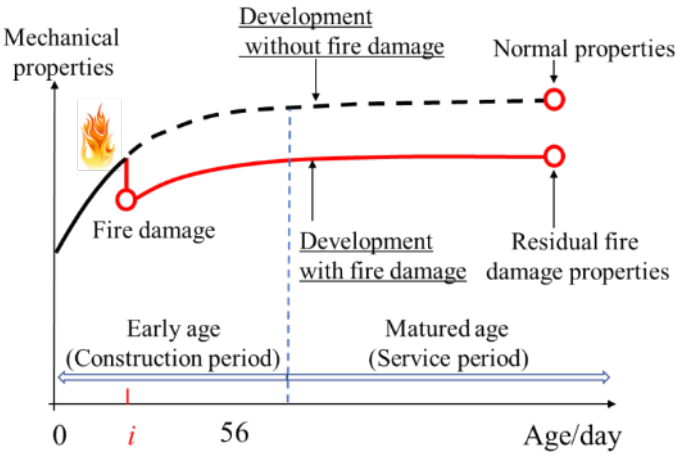


Figure 2 The influence of fire accident.

Ultra-high performance concrete (UHPC) is a durable, low-porosity cement-based material that reduces demand for concrete consumption and extends structure lifespan, thus lowering costs, energy consumption, and $CO_2$ emissions, rendering it a sustainable and versatile material for construction applications[5, 6]. Post-fire mechanical properties of UHPC have direct impacts on the post fire performance of a structure. Extensive research has been carried out worldwide on this topic. For example, researchers conducted high-temperature loading tests, focusing on the impact of curing methods, types of fibers, and content of coarse aggregates, etc. on the post-fire mechanical properties[7-11]. They employed techniques such as X-ray diffraction (XRD), scanning electron microscopy (SEM), mercury intrusion porosimetry (MIP), and computed tomography (CT) to understand the mechanisms of thermal degradation [12-14]. Post-fire stress-strain equations were proposed for direct design calculations[15, 16]. These studies provide scientific backing for advancing engineering applications of UHPC, refining designs, and addressing practical engineering challenges. While the behaviour of UHPC exposed to high-temperature during service has been extensively studied in the literature, there are only limited studies on the effects of fire on a structure during construction[17-20].

Concrete cast in the construction period is often in its early age and subjected to complex environmental and working conditions, such as temperature and curing conditions, impacting its mechanical performance. The damage caused by high temperatures at the early age is distinctly different from the damage that occurs during the service phase when exposed to high temperatures. However, research in this area remains limited. To the authors' knowledge, only a few researcher have conducted

relevant studies. For instance, Wang et al.[21] investigated the effect of fire damage at early age on the residual compressive strength of UHPC. However, Wang's study is limited to assessing fire damage at 28 days. Furthermore, the study focuses solely on compressive strength, overlooking other critical mechanical properties such as elastic modulus, peak strain, and stress-strain relationship. Building on Wang's research, Li[22] examined permeability of UHPC at 28 days. Additionally, Qian[23] studied the performance recovery of high-temperature damaged UHPC at early age under different curing environments by testing residual compressive and flexural strength of the UHPC that has endured high-temperature damage at 800 ℃ at 0, 14, and 28 days. Previous studies[24] have also investigated the effects of high-temperature curing(within 200 ℃) on the performance of UHPC. Overall, these studies only qualitatively examine the effects of temperature on the basic properties of UHPC of specific ages and temperature exposure, lacking a systematic and quantitative investigation into the combined effect of age and temperature on the residual performance of UHPC. Thus, there remains a significant research gap in the current literature regarding post-fire evaluation and repair strategies for structures exposed to fires during the construction phase, which is critical for assessing long-term safety performance of UHPC structures.

In order to fill the research gap, this paper presents uniaxial compressive test results of UHPC exposed to elevated temperature at early age. The test parameters include the age when they were exposed to elevated temperature, temperature, steel fiber content, and coarse aggregate. The failure modes, stress-strain curves, and key indicators such as compressive strength, elastic modulus, and peak strain were analyzed. Empirical stress-strain curve equations and expressions for key indicators for UHPC exposed to elevated temperature at early age are proposed. The degradation mechanisms of the UHPC exposed to elevated temperature at early age are studied through microscopic tests. This work provides a reference for fireproof design and safety assessment of UHPC structures throughout their lifecycle, contributing valuable insights for its application in fire-exposed construction scenarios.

# 2 Experimental program

## 2.1 Raw material and mix design

In the preparation of UHPC, materials were selected to ensure best possible strength and durability of the final mix. Among them, P.I. 52.5 Portland cement, silica fume, and fly ash were used as the binder. The water-to-binder ratio was uniformly set as 0.17. Specifically, Portland cement with a grade of 52.5 and a density of 3.20 g/cm³ was selected for its high strength. The measured compressive strengths of OPC at 3

days and 28 days were 34 MPa and 62 MPa, respectively, and the flexural strengths at 3 days and 28 days were 6.8 MPa and 9.2 MPa, respectively. Silica fume, with 95% $SiO_2$ content and a 125% activity index, was used to enhance the mix's cohesiveness and improve the pore structure of the UHPC. Fly ash from Henan Borun Casting Material Co., Ltd., with a density of 2.55 g/cm³, was used. The chemical composition of the cementitious materials was determined using an X-Ray Fluorescence Spectrometer through a standardless quantitative analysis method, and the results are presented in Table 1. The morphology of the cementitious materials was observed through scanning electron microscopy (SEM), the representative images of which are shown in the Figure 3.

Table 1 Chemical components of OPC, silica fume and fly ash（%）

| Chemical components | $Na_2O$ | MgO | $Al_2O_3$ | $SiO_2$ | $SO_3$ | $Fe_2O_3$ | $P_2O_5$ | CaO | $K_2O$ | MnO | ZnO | SrO |
|---|---|---|---|---|---|---|---|---|---|---|---|---|
| OPC | 0.079 | 2.14 | 4.5 | 19.58 | 3.06 | 3.119 | 0.128 | 64.94 | 0.75 | 0.127 | 0.024 | 0.148 |
| Silica fume | 0.068 | 0.224 | 0.354 | 95 | 1.26 | 0.113 | 0.11 | 0.213 | 0.332 | 0.008 | 0.019 | 0.005 |
| Fly ash | 0.552 | 0.575 | 30.63 | 48.74 | 0.706 | 2.611 | 0.247 | 2.44 | 1.25 | 0.016 | 0.013 | 0.060 |

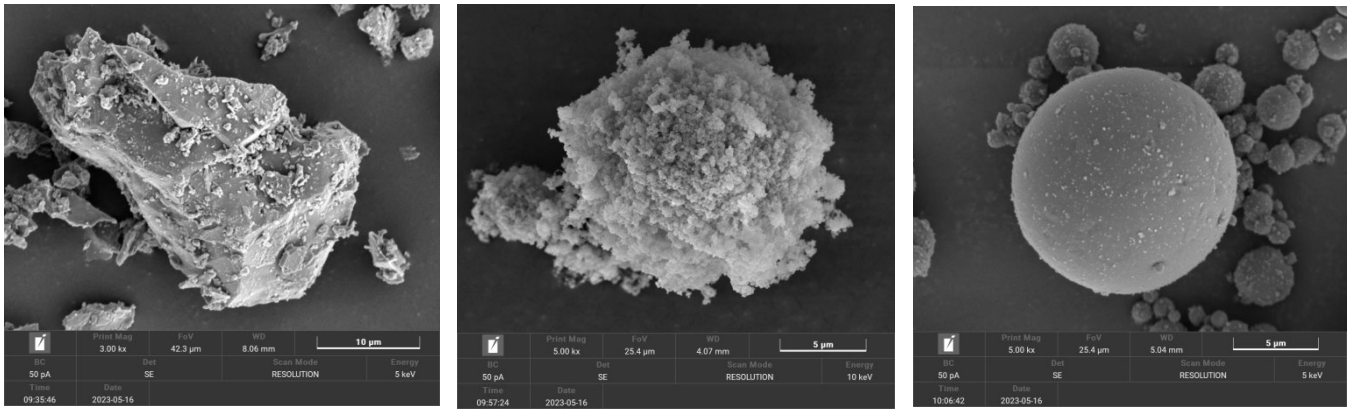

a) OPC　　b) Silica fume　　c) Fly ash

Figure 3　SEM images of OPC, silica fume and fly ash

Fine quartz sand with an average particle size of approximately 250 μm and basalt coarse aggregate of 5-10 mm were selected as the fine aggregate and coarse aggregate (CA), respectively. Copper-coated micro-wire steel fibers of 13 mm in length with an elastic modulus of 200 GPa were added to enhance ductility and reduce the possibility of undesired failure modes. Polypropylene fibers of 12 mm in length and an elastic modulus of 4.24 GPa were added to the mix to prevent explosive spalling at high temperatures[14, 25]. The mixture also contained tap water and high-performance powder polycarboxylate superplasticizer, which reduced the water content in the concrete by 29%. The mix proportions and

properties of the UHPC are listed in Table 2.

Table 2 Mix proportions and properties of UHPC (kg/m$^3$)

| Mix No | Mix proportions | | | | | | | | | Properties | | |
|---|---|---|---|---|---|---|---|---|---|---|---|---|
| | Matrix | | | | | | Admixture component | | | Cube strength (MPa) | Mass density Kg/m$^3$ | Moisture content % |
| | Cement | Silica fume | Fly ash | FA | PPF | Water | PPF | SF | CA | | | |
| S0CA0 | 877 (0.8) | 110 (0.1) | 110 (0.1) | 1206 (1.1) | 12 (0.01) | 186 (0.17) | 1.84 (0.2%) | 0 | 0 | 103 | 2495 | 2.83 |
| S1CA0 | 867 (0.8) | 108 (0.1) | 108 (0.1) | 1190 (1.1) | 12 (0.01) | 184 (0.17) | 1.84 (0.2%) | 78.5 (1%) | 0 | 110 | 2532 | 2.31 |
| S2CA0 | 858 (0.8) | 107 (0.1) | 107 (0.1) | 1179 (1.1) | 12 (0.01) | 182 (0.17) | 1.84 (0.2%) | 157 (2%) | 0 | 121 | 2554 | 2.10 |
| S2CA15 | 726 (0.8) | 91 (0.1) | 91 (0.1) | 998 (1.1) | 10 (0.01) | 154 (0.17) | 1.84 (0.2%) | 157 (2%) | 375 (15%) | 127 | 2604 | 2.36 |
| S2CA30 | 594 (0.8) | 74 (0.1) | 74 (0.1) | 817 (1.1) | 8 (0.01) | 126 (0.17) | 1.84 (0.2%) | 157 (2%) | 750 (30%) | 131 | 2652 | 2.01 |

Note: FA - fine aggregate, CA - coarse aggregate, SF - steel fiber, PPF - polypropylene fiber, and SP - superplasticizer.

Using the same UHPC mix[26-29], this study prepared five types of UHPC, including three volumetric ratios of steel fibers (0%, 1%, and 2%) and three volumetric ratios of coarse aggregates (0%, 15%, and 30%). The mix designs are denoted as 'SiiCAjj', where 'S' signifies steel fiber and 'ii' denotes fiber volume fraction. 'CA' stands for coarse aggregate, with 'jj' representing its volume fraction. Detailed mix proportions are presented in Table 2. As shown in Figure 4, the specimens were subjected to 200°C, 400°C, 600°C and 800°C at different early ages (3, 7, 14, 28, and 56 days) and loaded on the 60th day.

In the existing literature, the timeframe defined for "early age " of concrete ranged generally from 1 to 180 days, depending on specific research and concrete type[30, 31]. Apart from the simple time-based definition, Bergstrom proposed that "early age " could also be characterized as the period before a given performance criterion reaches the specified requirements for use[32]. Given that this study examines high-temperature performance under fire exposure, we adopted this performance-based definition of early age. It was observed from our tests that the mechanical properties of the UHPC became relatively stable after 56 days of age. Thus, in this study concrete under 56 days old was classified as early age, which agrees with the observations from previous studies[33]. Without being exposed to high temperature, the specimen made from matured UHPC (older than 56 days) at room temperature was used as the control group (CG.), which is considered to represent mature UHPC in its service period. All specimens were cured at room temperature in a confined space, simulating the real application environment, such as in steel tube UHPC structures. A total of 105 groups of cylindrical specimens (φ100 mm × 200 mm) were prepared for the axial compressive tests. There were three specimens of the same mix design in each of the groups.

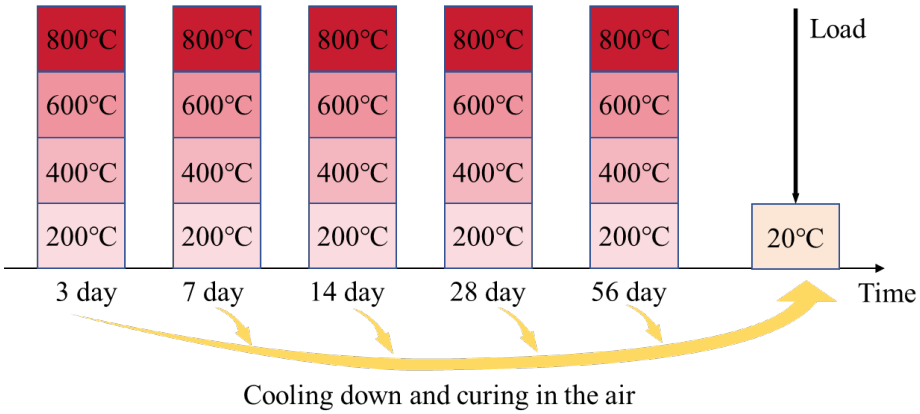


Figure 4 Specimen design

## 2.2 Preparation of specimens

The UHPC was cast using a 120 L vertical axis planetary mixer, as shown in Figure 5. Initially, the required amounts of quartz sand, coarse aggregate, P.O.52.5 cement, silica fume, fly ash, and superplasticizer were weighed and mixed continuously for 5 minutes. Next, water and polypropylene fibers were measured and mixed together thoroughly. The wet fibres were then divided into three equal portions, which were subsequently added to the cement mixer at one-minute interval. The total mixing time was 5 minutes. Finally, steel fibers were added into the rotating mixer that ran for an additional 5 minutes. The fresh concrete was then poured into plastic molds treated with release agent. The cast cement was vibrated on a shaking table for 30 seconds and the surface was levelled with a trowel. To prevent moisture loss, the specimens were covered immediately with plastic film.


Figure 5 The process of fabrication of tested specimens

## 2.3 High temperature treatment

As shown in Figure 6, the specimens were subjected to a controlled heating process in a ZX-DY-JDQ02 electric kiln furnace. From the literature review and our preliminary tests, it was found that the UHPC was likely to burst at a temperature between 100 °C and 400 °C[14]. To prevent bursting and ensure

valid mechanical property assessments, the temperature was raised by an increment of 100°C up to 400°C and kept constant at each of the increments for 1.5 hours. This heating regime aimed to reduce temperature gradients and thermal stresses. To facilitate more effective vapor release, h a general heating rate of 1°C/min was followed. Once the target temperature was reached, it was maintained for 3 hours to achieve a near uniform temperature field within the specimens before allowing the furnace to cool naturally.

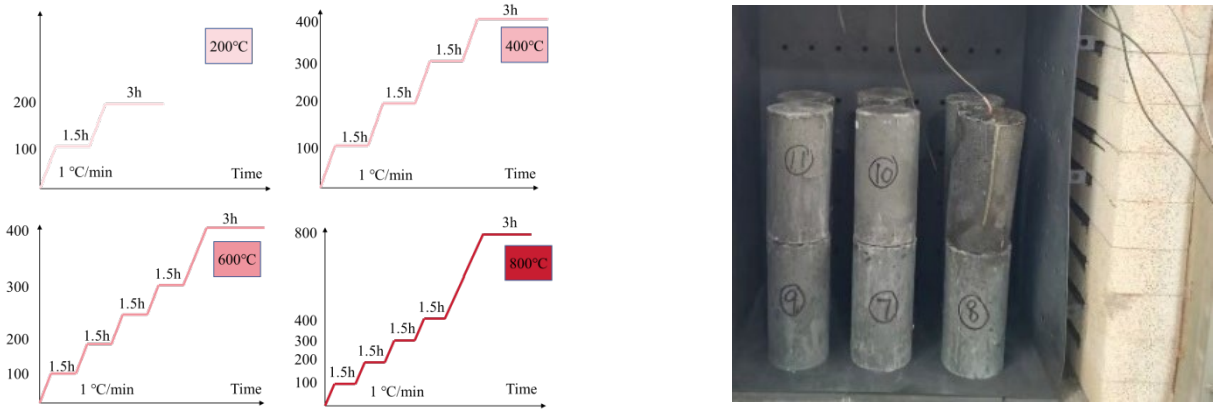


a) Heating system b) Heating process

Figure 6 High temperature treatment

## 2.4 Mechanical tests

As shown in Figure 7, the uniaxial compressive strength tests were conducted on 100 × 200 mm cylindrical specimens using an MTS electro-hydraulic servo material testing machine with a capacity of 2500 kN. To ensure even force distribution, the loading surfaces of the specimens were leveled with ultra-hard gypsum. After aligning a specimen for pre-loading, a 1kN force was applied to generate initial contact, followed by a displacement-controlled pre-load of 10%–20% of the expected compressive strength. The following loading proceeded at 0.002 mm/s until the peak strain was reached approximately. During the loading process, deformation of the specimen was measured using a Linear variable displacement transducer (LVDT) and a digital image correlation (DCI) system. To mitigate the end effects, measurements were taken from the middle 100 mm range of the specimen.

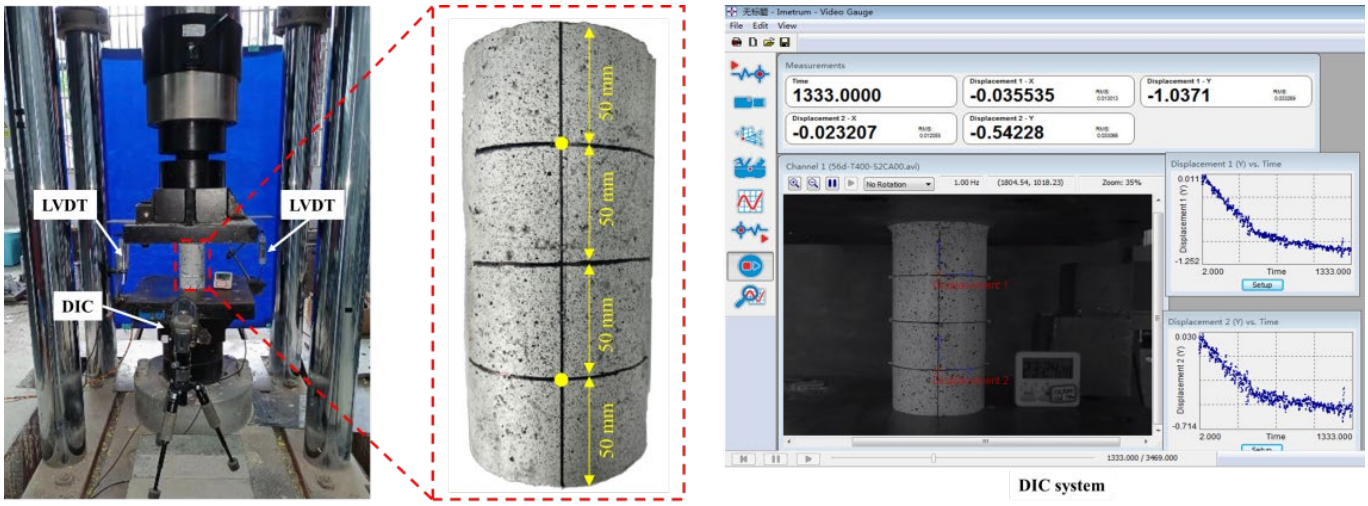


Figure 7 Mechanical tests

## 2.5 Microscopic tests

As shown in Figure 8, to investigate the surface morphology and the microstructure of the UHPC samples after exposure to high temperature, samples were taken first from the fractured cylinders. Fragments of approximately 5 mm in diameter and 3 mm in thickness were then immersed in anhydrous ethanol for 48 hours before being dried in a vacuum oven at 60°C for 48 hours until there was no further mass reduction. This procedure was employed to prevent further hydration of the UHPC by removing as much internal moisture as possible[34], thereby minimizing discharge phenomena during SEM examination. The samples were stored in sealed bags to prevent further water absorption and carbonation. Prior to examination, to mitigate the charging effects that can interfere with imaging process during the electron microscopy, the UHPC fragments were adhered to the sample holder using conductive adhesive and coated with gold using ion sputtering. Finally, the surface morphology and the microstructure of the samples were analyzed using the SEM, a tungsten filament scanning electron microscope (CLARA GMH) The operation was completed at an accelerating voltage of 0.5 to 30 kV with a resolution of 0.9 nm and a probe current range of 2 pA to 400 nA, and has achieved a maximum magnification of 2,000,000x.

To identify the crystalline phases present in the samples and their relative contents, XRD tests were conducted. To avoid the diffraction peaks of quartz sand and other substances overshadowing the hydration products of UHPC, the tests were performed on the paste without sand. Initially, small pieces of the paste samples were ground with the assistance of anhydrous ethanol. Then, the supernatants were extracted with a dropper and dripped into a glass vial. Once the solid powder in the vial was completely settled, it was subsequently dried in a vacuum oven at 40°C for 48 hours. The powder was then analyzed using XRD

(Bruker D8 ADVANCE). The primary configuration included a Cu-target X-ray tube, a ceramic X-ray tube (2.2 kW), an optical system, a slit system, a standard sample stage, a goniometer, and a Lynxeye XET two-dimensional detector. The $2\theta$ rotation range is from -110° to 168°, and the goniometer radius is 270 mm, allowing for a continuously variable diameter of the goniometer circle. The minimum readable step size is 0.0001°, with an angular reproducibility also at 0.0001°. The Lynxeye XET detector is suitable for both small- and wide-angle measurements.

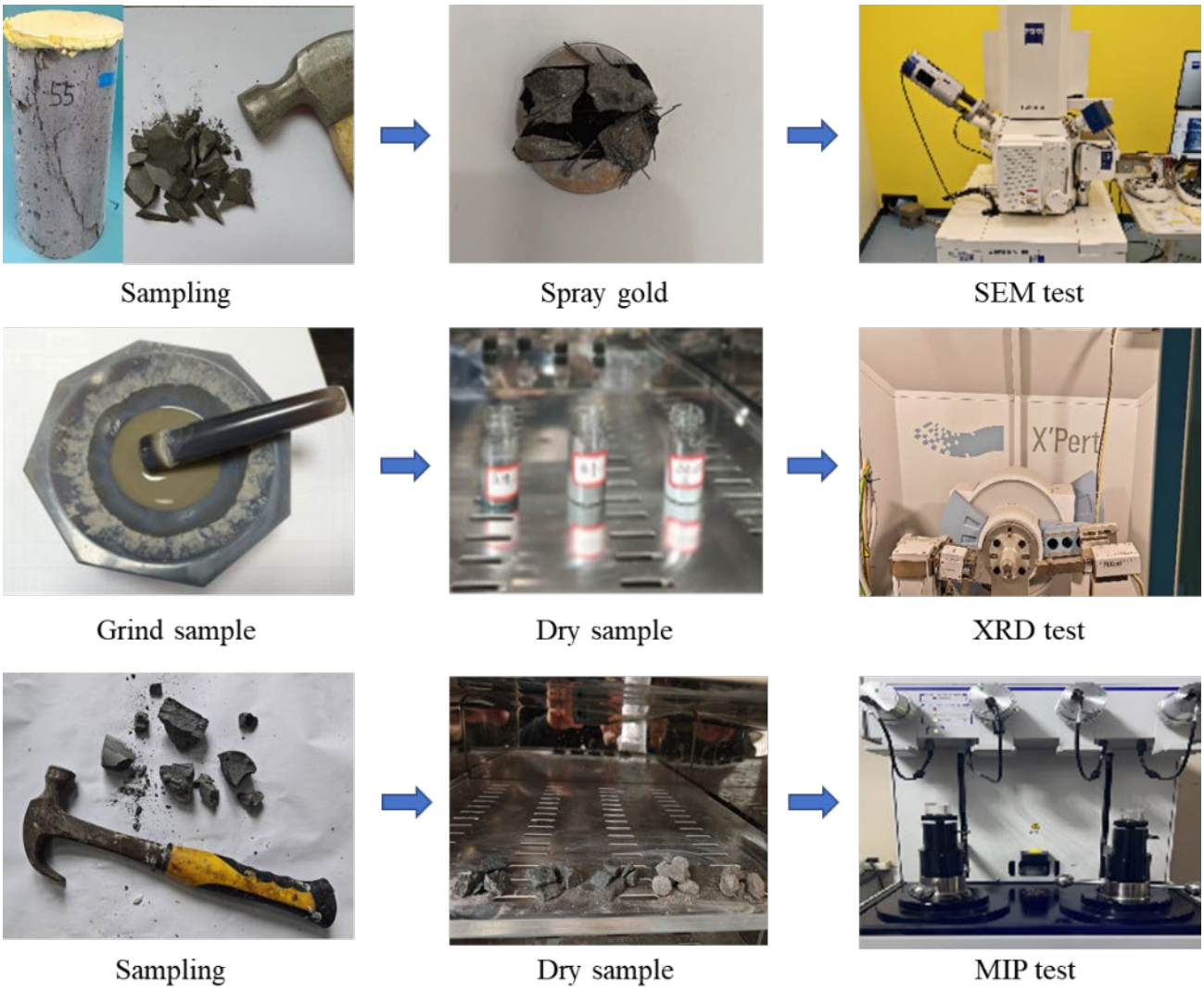


Figure 8 The process of the microscopic tests

The porosity and pore size distribution of the samples were measured using mercury intrusion porosimetry (MIP). The specimens were cut from $\varphi$100×200 mm cylindrical blocks subjected to high temperatures at various ages, yielding cubic samples with a maximum length of approximately 10 mm. To minimize heating during the cutting process, the samples were continuously cooled down with sprinkle water. After cutting, the samples were promptly immersed in isopropanol and cleaned using an ultrasonic

cleaner. After two hours, the samples were dried in an oven at 80°C for 24 hours. The pore structure was subsequently analyzed using the AutoPore V automated mercury porosimeter, which is capable of measuring pore diameters ranging from 0.003 to 1100 micrometers.

# 3 Mechanical analysis

The experimental results of all the specimens are evaluated in this Section, including failure modes, stress-strain curves, key indicators such as compressive strength, elastic modulus, and peak strain. It should be noted that the presented results are the group averages of the tests. The error bars in the figures show the standard deviation of the test results of each group.

## 3.1 Failure mode

Figure 9 presents the failure modes of the tested specimens. It can be found that the failure morphology of the UHPC is influenced by the amounts of steel fibers and coarse aggregate. The temperature also plays a crucial role, while the age of the concrete has minimal impact on the failure morphology. Specifically, an increase of the amount of steel fibers typically enhances structural integrity of the specimens, demonstrating that the fibers have strengthened the overall structure. The specimens with lower or no steel fibers (such as S0CA00 and S1CA00) mainly exhibit brittle splitting failure at all temperature, whereas those with higher fiber content tend to show shear failure characterized by more ductile damage. The addition of coarse aggregate leads to more fine cracks around the main diagonal crack. At 200°C and 400°C, the specimens mostly display brittle failure. However, at 600°C and 800°C, except for those with no or low fiber content, the specimens exhibit more ductile damage. At 800°C, oxidation of steel fibers and crumbling of the matrix significantly alter the damage morphology. However, the age exposed to elevated temperature has minimal influence on the failure mode, indicating that the failure morphology of the UHPC is primarily determined by the micro-composition of the materials and the thermal conditions.

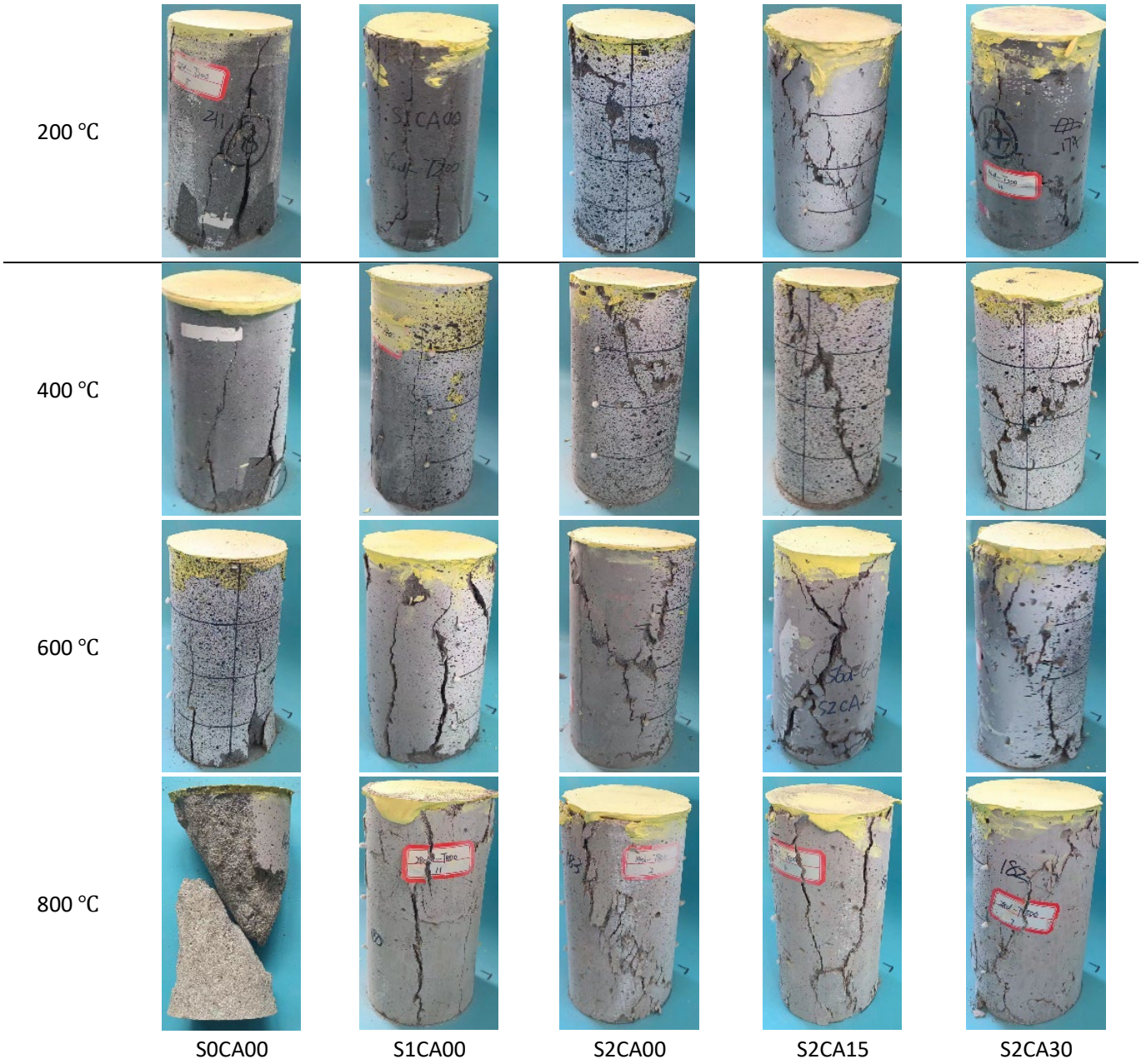


Figure 9 Failure mode of the partial specimens

### 3.2 Stress-strain curves

Figure 10 presents the full stress-strain curves of the UHPC mixtures under uniaxial compression when they are subjected to the same temperature at different ages. It can be observed that the age exposed to elevated temperature has little effect on the shape of the stress-strain curves. However, the temperature significantly affects the curves. Specifically, after exposure to 200°C, 400°C, and 600°C, a noticeable sharp drop of the curve occurs after the peak point, indicating pronounced brittleness. However, after exposure to 800°C, the curves descend gradually after the peak point, showing reduced brittleness. It can be seen also that the incorporation of steel fibers and coarse aggregates enhances the strength and ductility of the UHPC.

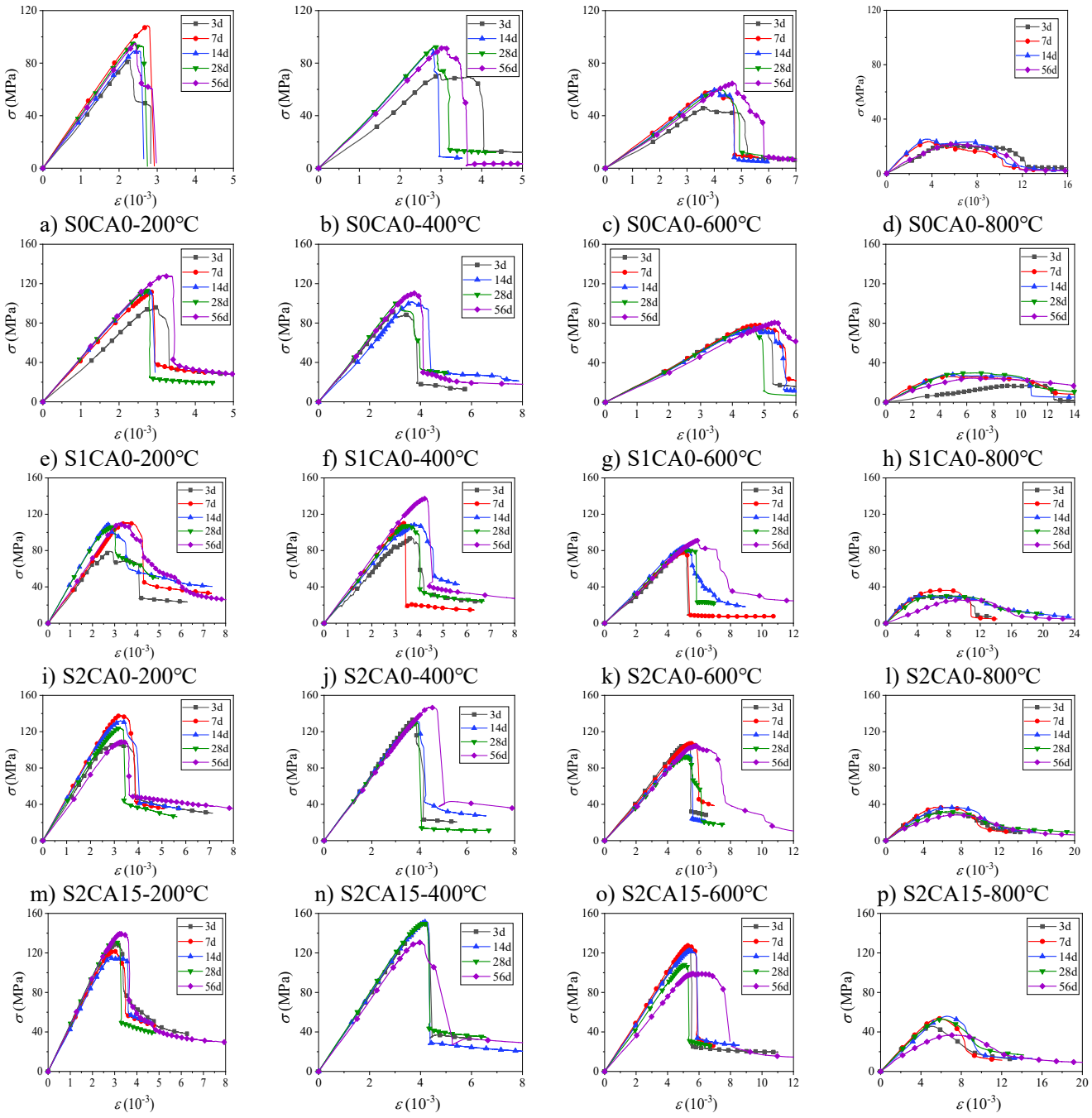


Figure 10 Stress–strain curves of UHPC exposed to elevated temperature at different early age

## 3.3 Analysis of featured indicators

To further study the mechanical properties of the UHPC specimens exposed to elevated temperatures at different early ages, the effects of various factors on the elastic modulus, peak stress, and other key properties of the specimens observed from the stress-strain curves in Section 3.2 are studied in this section.

### 3.3.1 Compressive strength

Figure 11 displays the variation of the compressive strength of the UHPC with different mixes at

various ages after exposed to elevated temperature. In the bar chart, CG. is the strength of the matured UHPC of the control group at room temperature, and the others are the residual strength after exposure to elevated temperatures at different age. The other figures show the relative strength, defined as the ratio of the compressive strength of the specimens exposed to elevated temperature at early age to that of the same specimens at room temperature, against either temperature ($T$) and or age ($t_T$) when exposed to elevated temperature.

The results show that the residual strength of the UHPC demonstrates an overall increasing trend as the temperature rises from ambient to 400°C. However, some specimens exhibit a decrease in strength around 200°C. This can be attributed to the evaporation of free water starting at approximately 100°C, which leads to the formation of capillary cracks and pores, thereby generating tension in the surrounding medium and resulting in a reduction of compressive strength[9]. Throughout this process, the escaping steam acts similarly to "self-curing," promoting further hydration of the cement particles, which in turn enhances compressive strength[35]. The effects of hydration and the tension generated by evaporation exhibit considerable variability. For some specimens, the effect of hydration at 200°C may be less significant than the tension induced in the medium, resulting in a slight decrease in strength. Conversely, if hydration is more dominating, strength may increase. In the temperature range from ambient to 400°C, hydration plays a dominant role, leading to a clear upward trend in strength as the temperature rises. When the temperature is between 400°C and 600°C, some internal hydration products, such as CH ($Ca(OH)_2$, calcium hydroxide) , begin to dehydrate and decompose from around 530°C, causing concrete shrinkage and cracking. Additionally, the partial decomposition of C-S-H (Calcium silicate hydrate) gel and the loss of crystalline water lead to the formation of capillary pores and cracks that are further expanded by the internally accumulated steam[36]. As the temperature increases to between 600°C and 800°C, the compressive strength of the UHPC is significantly reduced, primarily due to the dehydration of the C-S-H gel.

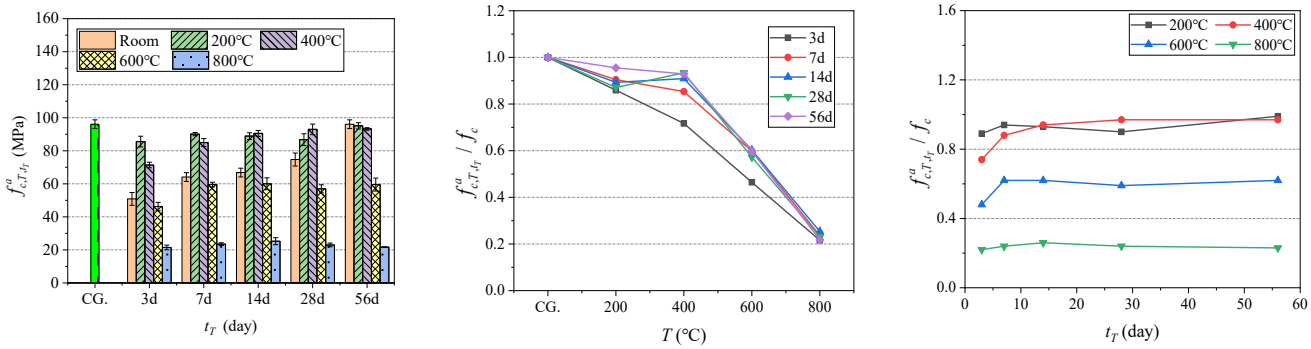

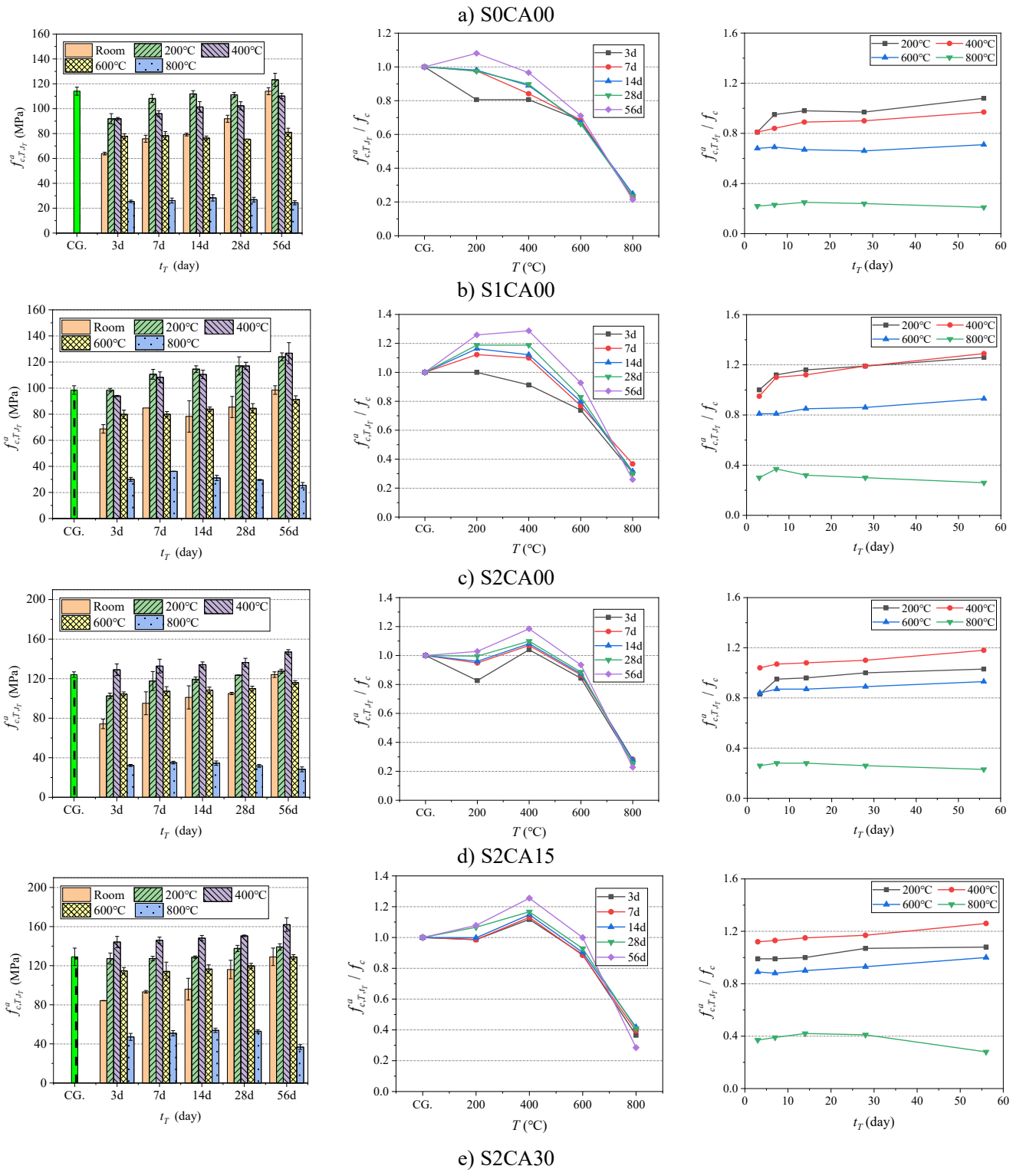


Figure 11 Residual cylinder compression strength of UHPC exposed to elevated temperature at different early age

It can be seen from Figure 11 that the development of strength of the specimens exposed to elevated temperatures at early ages is comparatively limited when compared with the development at room temperature. This is attributed to that the younger specimens, which possess lower degrees of initial hydration and higher water content, provide a more favorable environment for pozzolanic reactions that result in a more significant enhancement in performance when they are exposed to elevated temperature.

Consequently, this narrows the gap between these specimens and those with a older age of UHPC. However, a closer analysis reveals that the age of the UHPC specimens at the time of exposure to elevated temperatures still has a notable effect on their residual compressive strength. When the exposed temperature is below 600°C, the residual compressive strength of the UHPC generally shows an upward trend with the increase of the age. This trend occurs because the older UHPC specimens contain higher amounts of C-S-H gel from natural hydration. This observation is further supported by the X-ray diffraction analysis discussed later. However, there is a slight decrease in strength at 800°C, likely due to that the UHPC matrix becomes more porous and looser, facilitating carbonation reactions with the water and $CO_2$ in the air[37], which temporarily enhances its strength.

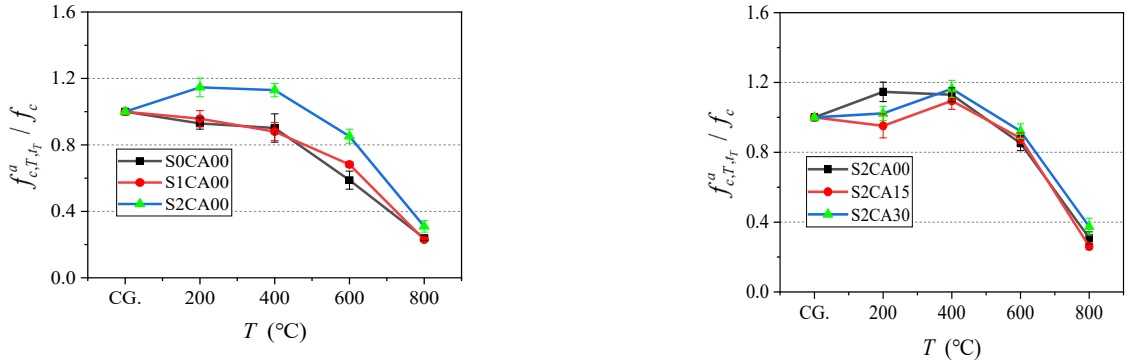


a) Steel fiber b) Coarse aggregate

Figure 12 The influence of steel fiber and coarse aggregate on the residual strength

Figure 11 demonstrates that the relative compressive strength of the UHPC with the same mix ratio are similar across all different age groups when they are subjected to the same high temperatures. Therefore, the average relative strength across all different age groups are calculated to analyse the effects of steel fibers and coarse aggregates on the residual strength. As shown in Figure 12, the UHPC specimens with 2% steel fibers show a higher residual compressive strength and a superior high-temperature resistance. The good thermal conductivity of the steel fibers helps to reduce the temperature difference over the cross-section, thereby reducing microcracks caused by thermal stress and helping to reduce cracking caused by concrete expansion[38]. The incorporation of coarse aggregate results in more interfaces between the aggregate and the matrix within the UHPC specimens, where the differences in thermal deformation introduce cracking, thus increasing high-temperature deterioration.

### 3.3.2 Elastic modulus

Figure 13 shows the variation of elastic modulus of the UHPC with different mixes at various ages

after exposure to elevated temperature. The bar chart presents the elastic modulus of the matured control group at room temperature (CG) alongside the residual elastic modulus after exposure to elevated temperatures at different ages. It also illustrates the relative elastic modulus, defined as the ratio of the elastic modulus at early age exposure to that at room temperature, plotted against temperature ($T$) or ages ($t_T$). It is observed that the elastic modulus consistently decreases with the increase of temperature, which differs from the compressive strength of the UHPC, where an initial increase is followed by a subsequent decline. This suggests that the elastic modulus is more sensitive to elevated temperatures. Below 400°C, the high-temperature and high-pressure steam inside the UHPC promotes the formation of C-S-H gel. However, the newly formed hydration products cannot fully occupy the pores and cracks caused by high temperatures. Compared to strength, the further development of microcracks under high temperatures has a more significant negative impact on the elastic modulus. Above 400°C, as the temperature increases further, the internal pores and cracks in the UHPC increase and the structure coarsens, further reducing the elastic modulus. This has also been verified in subsequent mercury intrusion porosimetry tests. As a result, the elastic modulus of the UHPC exposed to elevated temperatures across different ages is consistently lower than that of the matured UHPC at ambient conditions.

It also can be seen from Figure 13 that the elastic modulus of the UHPC at or below 400°C generally shows an upward trend with the increase of age exposed to elevated temperature. Above 400°C, the elastic modulus shows no significant change or a slight decrease with increasing age exposed to elevated temperature. After exposure to 600°C, the steam pressure environment enhances hydration and pozzolanic reactions, possibly increasing the elastic modulus of early aged UHPC due to the production of more hydration products, while the UHPC aged longer exhibits stronger resistance to high temperatures, keeping the elastic modulus relatively stable. After exposure to 800°C, the UHPC becomes more porous, which accelerates carbonation. An earlier exposure of the UHPC to high temperature lead to longer period of carbonations, thereby somewhat enhancing the elastic modulus of the material.

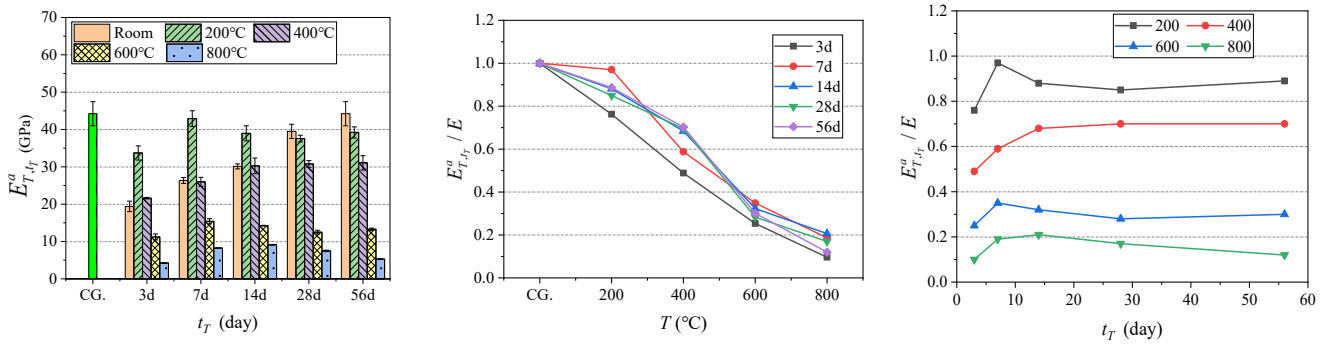


a) S0CA00

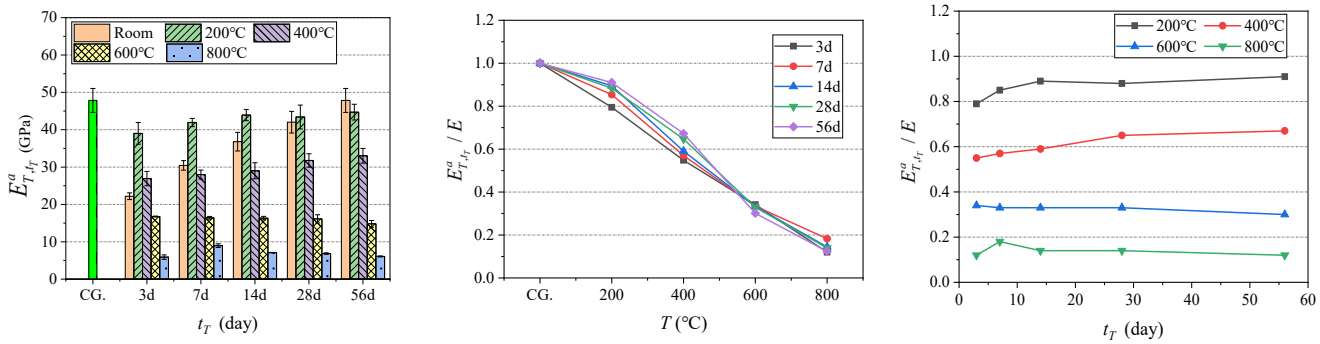


b) S1CA00

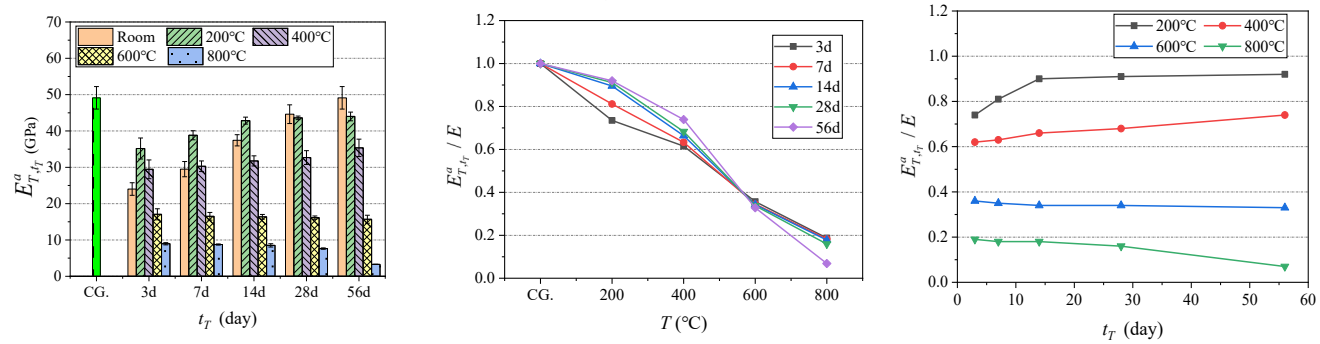


c) S2CA00

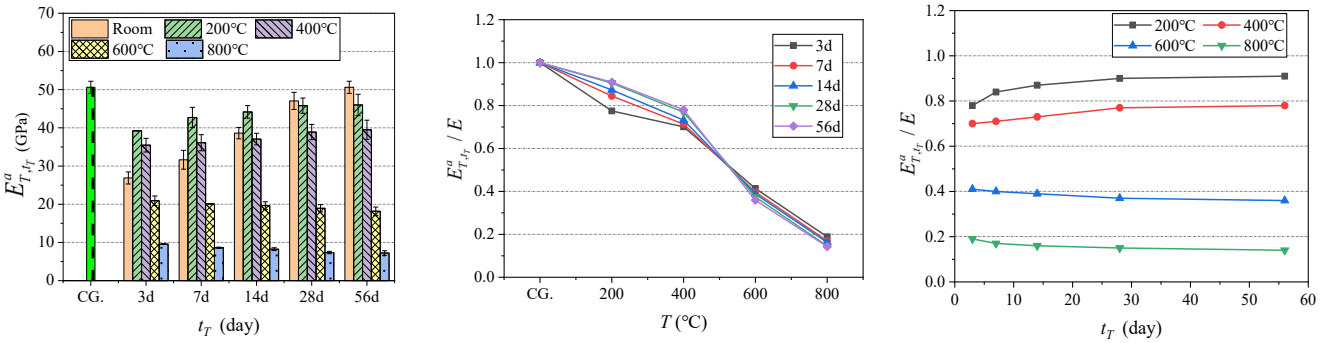


d) S2CA15

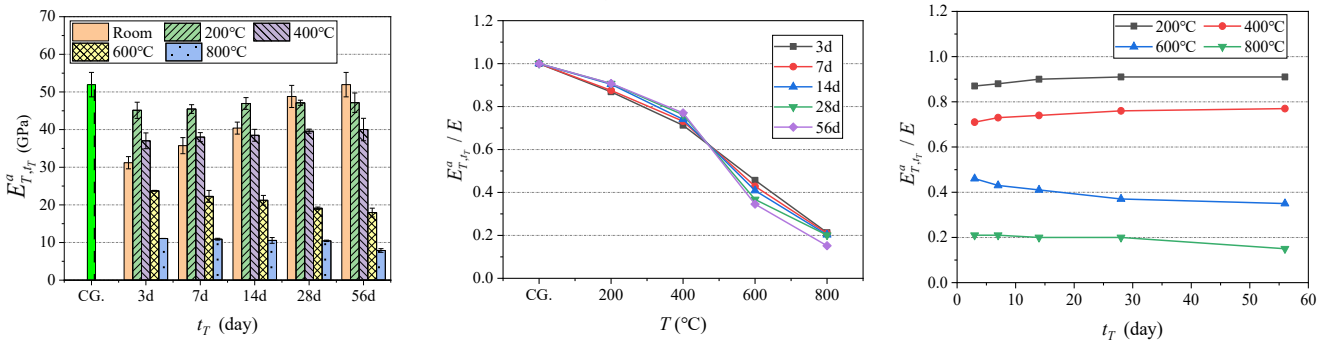


e) S2CA30

Figure 13 Elastic module of UHPC exposed to elevated temperature at different early age

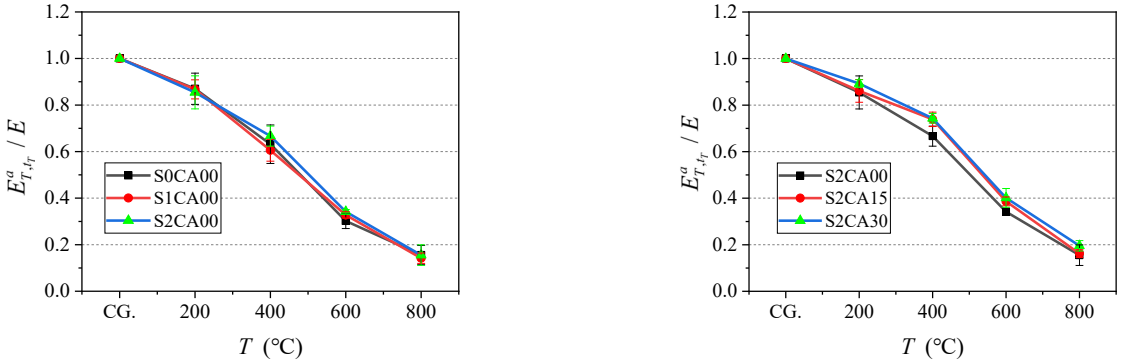


a) Steel fiber b) Coarse aggregate

Figure 14 The influence of steel fiber and coarse aggregate on elastic module

From Figure 13, it is evident that the age exposed to elevated temperature has a minimal impact on the elastic modulus of the UHPC when they are subjected to the same temperature.

The relative elastic module of the UHPC with the same mix and temperature but different ages exposed to elevated temperature are averaged to reflect the influence of the steel fibers and coarse aggregate on the relative elastic modulus, which are presented in Figure 14. It can be observed that the presence of steel fibers has a negligible effect on the relative elastic modulus. This is likely because the volume of steel fibers is small and their impact is significant only at the initial compression stage. Additionally, the introduction of coarse aggregate enhances the relative elastic modulus of the UHPC. The properties of coarse aggregates are relatively stable and less affected by high temperature. Given their higher content, the inclusion of coarse aggregates effectively mitigates the degradation of the elastic modulus.

### 3.3.3 Peak strain

Figure 15 presents the variation of peak strain and the relative peak strain, with the latter defined as the ratio of peak strain for specimens exposed to elevated temperatures at different ages to that of matured UHPC at room temperature. It is observed that the peak strain of the UHPC generally increases with rising temperatures. This increase is attributed to increased porosity and crack formation within the UHPC specimens, leading to coarsening of the pore structure and reduced cohesion between matrix components, thereby increasing the deformability of the specimens. Notably, the peak strains at 800℃ for the specimens without coarse aggregate at 7 and 14 days are lower than that of those at 600℃, possibly due to the reduced deformability of the UHPC attributable to the effect of sintering.

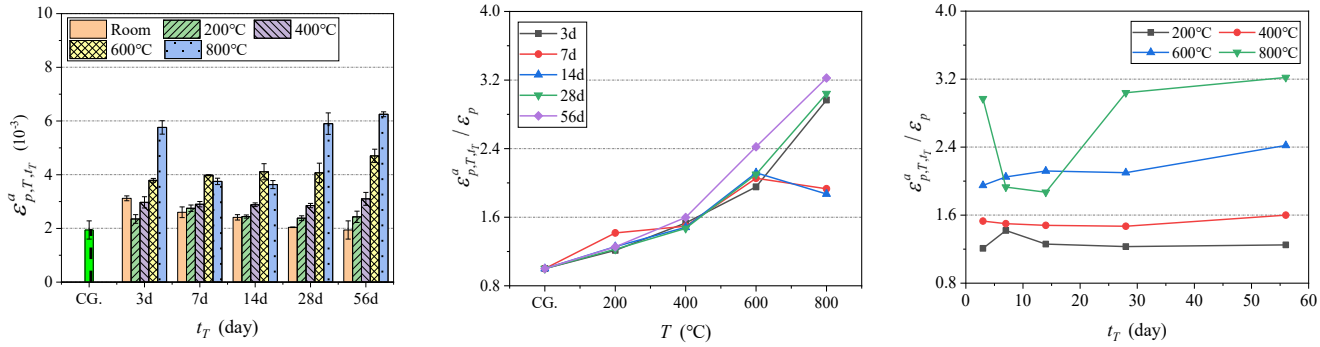


a) S0CA00

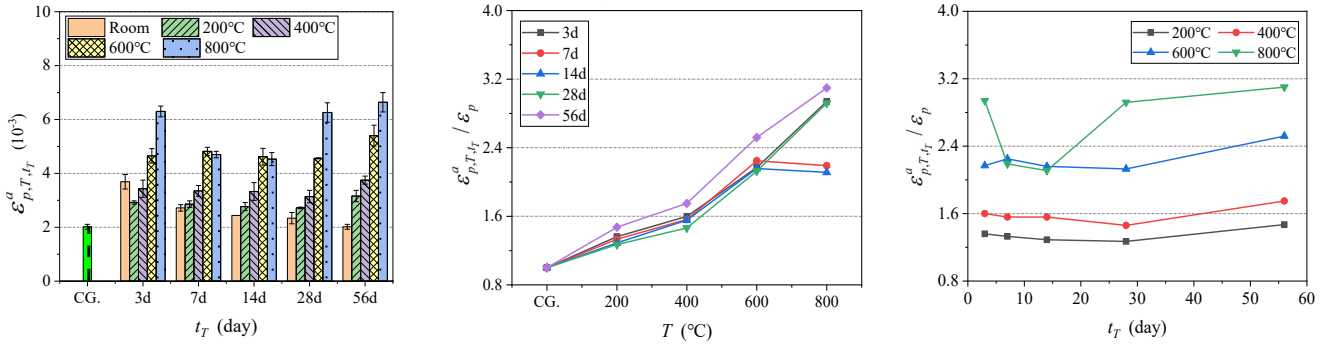


b) S1CA00

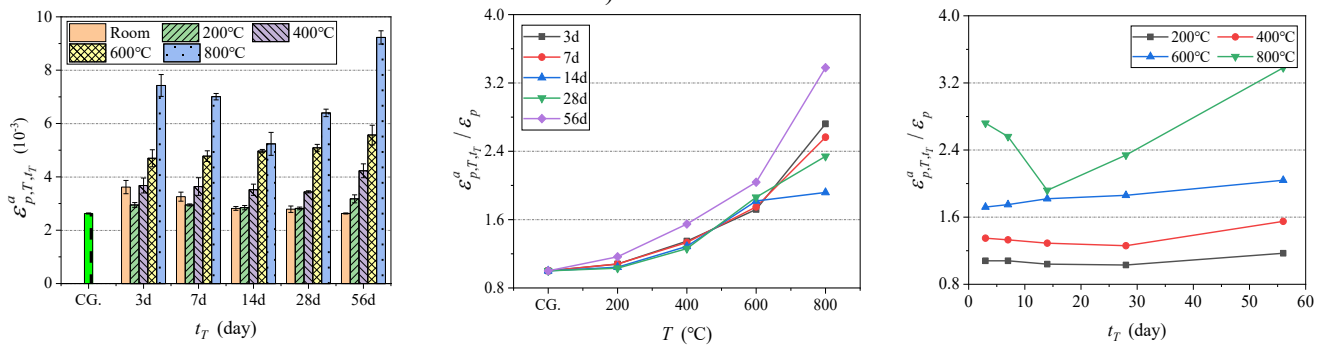


c) S2CA00

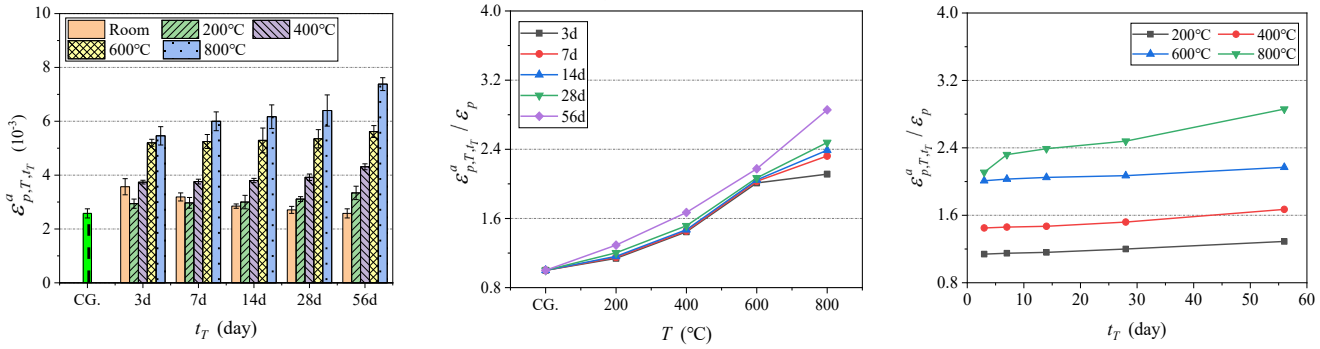


d) S2CA15

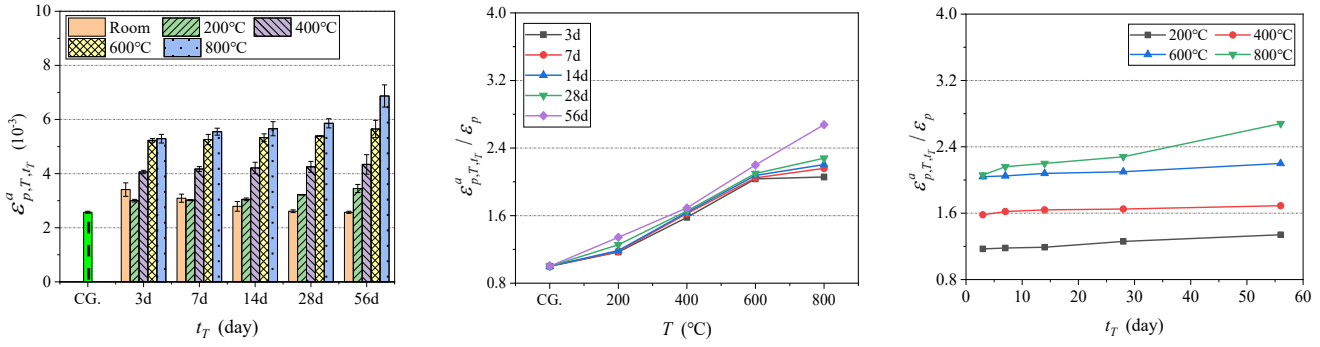


e) S2CA30

Figure 15 Peak strain of UHPC exposed to elevated temperature at different early age

Regarding the influence of age, the peak strain of the UHPC shows a slightly upward trend with the increase of the age exposed to elevated temperature. This trend may be explained by the fact that UHPC specimens exposed to high temperatures at earlier ages have longer exposure to atmospheric $CO_2$ during subsequent natural resting periods, leading to a higher degree of carbonation. Existing research has confirmed that carbonation contributes to increased concrete brittleness, thereby reduced deformability[39]. Consequently, the peak strain of the UHPC exposed to elevated temperature at early age is lower than that of the mature UHPC exposed to high temperatures at a later stage.

It can be found also that the peak strain of the specimens without coarse aggregate at 7 and 14 days after exposure to 800°C is less than that at 600°C. This may be due to the weakened deformation capacity of the UHPC caused by sintering[40]. When the temperature reaches 575°C, the siliceous aggregate undergoes a phase transformation, resulting in a volume expansion of 0.86%[41]. Therefore, after adding coarse aggregate, the deterioration of the UHPC exposed to 800°C is more significant, and the residual deformation is greater.

## 3.4 Unified calculation of post-fire residual stress–strain relations

### 3.4.1 Calculation of featured indicators

Based on the analyses above, it is evident that factors such as age of exposure to elevated temperature ( $t_T$) , temperature ( $T$ ), steel fiber content ($V_{sf}$ ), and coarse aggregate content ($V_{ca}$) significantly affect the residual compressive strength, elastic modulus, and peak strain of the UHPC. This section develops a mathematical expression to study further the influences of these factors.

The development of the expression includes two main steps, i.e., first, based on the featured indicators of the mortar (S0CA0) , the correction factors $k_{i,sf}$ and $k_{i,ca}$, where $i$ denotes a featured indicator, and takes $c$, $E$ and $p$ for strength, elastic module and peak strain, respectively, are introduced to account for the effects of steel fiber and coarse aggregate content ($V_{sf}$ and $V_{ca}$) .This is to obtain the characteristic indicators of different mix designs for matured UHPC at room temperature. Next, $k_{T,t_T}^{a}$ is introduced to consider the coupling effect between the age of exposure to elevated temperature ( $t_T$) and temperature ( $T$ ) on the matured UHPC at room temperature, and to derive the residual key indicators exposed to elevated temperatures at an early age. It should be noted that the modified expression for considering age and temperature must satisfy two conditions: 1) At room temperature (T=20°C), the modification parameter of temperature is 1, and the overall formula degenerates to the one for matured UHPC at room temperature;

2) At matured age ($t_T \geqslant 56$ days), the formula degenerates to the one for matured UHPC after exposure to high temperatures. Based on the experimental results and nonlinear programming analysis, the expressions for axial compressive strength, elastic modulus, and peak strain of UHPC at different ages after high temperature exposure are derived and presented in Table 3. Figure 16 compares the formula predictions with the experimental values, demonstrating a good overall agreement.

Table 1 The calculation of featured indicators

| Index | Main formulas | Sub-formulas | |
|---|---|---|---|
| Cylinder strength | $f^a_{c,T,t_T} = k^a_{c,T,t_T} \cdot f_c$ | $f_c = k_{c,CA} \cdot k_{c,S} \cdot f_{c0}$ | $k^a_{c,T,t_T} = 1 + \left(k^a_{c,T} - 1\right) \cdot k^a_{c,t_T}$ |
| | | $k_{c,ca} = 1 + 0.92V_{ca}$ | $k^a_{c,T} = -2.45\left(\frac{T-20}{1000}\right)^2 + 1.04\left(\frac{T-20}{1000}\right) + 1$ |
| | | $k_{c,sf} = 1 + 3.98V_{sf} - 2.45V_{sf}^2$ | $k^a_{c,t_T} = 1 - e^{-1.94t_T}$ |
| Elastic module | $E^a_{T,t_T} = k^a_{E,T,t_T} \cdot E$ | $E = k_{E,CA} \cdot k_{E,S} \cdot E_0$ | $k^a_{E,T,t_T} = 1 + \left(k^a_{E,T} - 1\right) \cdot k^a_{E,t_T}$ |
| | | $k_{E,ca} = 1 + 0.56V_{ca}$ | $k^a_{E,T} = -0.54\left(\frac{T-20}{1000}\right)^2 - 0.68\left(\frac{T-20}{1000}\right) + 1$ |
| | | $k_{E.sf} = 1 + 2.12V_{sf} - 2.63V_{sf}^2$ | $k^a_{E,t_T} = 1 - e^{-1.99t_T}$ |
| Peak strain | $\varepsilon^a_{p,T,t_T} = k^a_{\varepsilon,T,t_T} \cdot \varepsilon_p$ | $\varepsilon_p = k_{\varepsilon,CA} \cdot k_{\varepsilon,S} \cdot \varepsilon_{p0}$ | $k^a_{\varepsilon,T,t_T} = 1 + k^a_{\varepsilon,T} \cdot k^a_{\varepsilon,t_T}$ |
| | | $k_{\varepsilon,ca} = 1 - 0.15V_{ca}$ | $k^a_{\varepsilon,T} = 1.03\left(\frac{T-20}{1000}\right)^2 + 1.35\left(\frac{T-20}{1000}\right) + 1$ |
| | | $k_{\varepsilon,sf} = 1 + 13.12V_{sf}$ | $k^a_{\varepsilon,t_T} = 1 - e^{-1.12t_T}$ |

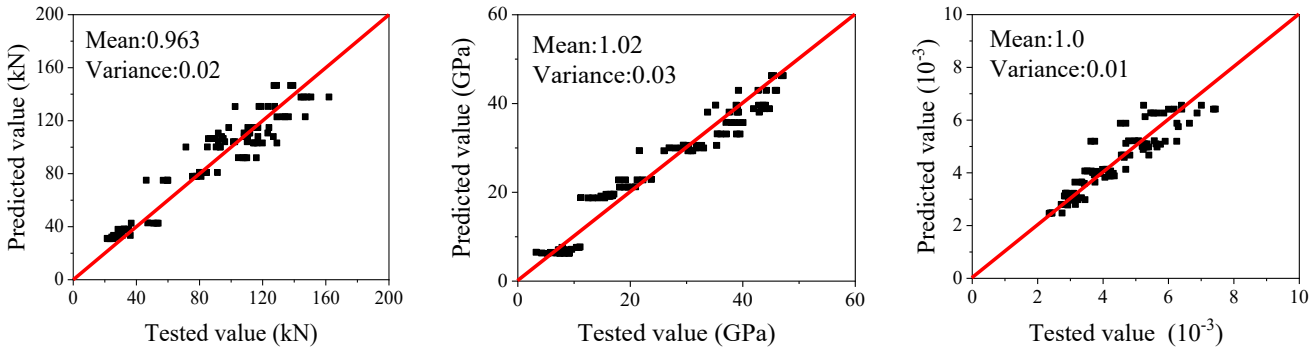


a) Cylinder strength b) Elastic module c) Peak strain

Figure 16 Validation of the compressive strength, elastic modulus and peak strain

### 3.4.2 Proposed stress–strain relations

In previous research, several analytical models[42-44] have been proposed to simulate experimental compression stress-strain curves of concrete. The Chinese code (GB50010[44]) provides the stress-strain relations shown in Eq.(1~2), which has been successfully applied to different kinds of concrete at room and

elevated temperatures[45-47].

$$y=\begin{cases}\dfrac{nx}{n-1+x^{n}} & (0\le x\le 1)\\ \dfrac{x}{\beta(x-1)^{2}+x} & (x>1)\end{cases} \tag{1}$$

$$n=\frac{E^{a}_{T,t_T}\varepsilon^{a}_{p,T,t_T}}{E^{a}_{T,t_T}\varepsilon^{a}_{p,T,t_T}-f^{a}_{c,T,t_T}} \tag{2}$$

where $x=\varepsilon_0/\varepsilon^{a}_{p,T,t_T}$, and $\varepsilon$ and$\varepsilon^{a}_{p,T,t_T}$ are compressive strain and peak strain, respectively; $f^{a}_{c,T,t_T}$ and $E^{a}_{T,t_T}$are strength and elastic module of the UHPC exposed to elevated temperature at early age, respectively. $\beta$ is an independent factor that is associated with the shape of the descending branch of the curve.

In this study, the ascending phase of the curve (for $x \le 1$) from the Chinese code (GB50010[44]) is directly adopted. However, the descending phase of the curve (for $x>1$) is modified. This phase is governed by the independent factor $\beta$, which is positively correlated with strength[47]. The relationship between $\beta$ and strength is established through data regression, as expressed in Eq.(3).

$$\beta=0.00097(f^{a}_{c,T,t_T})^{2} \tag{3}$$

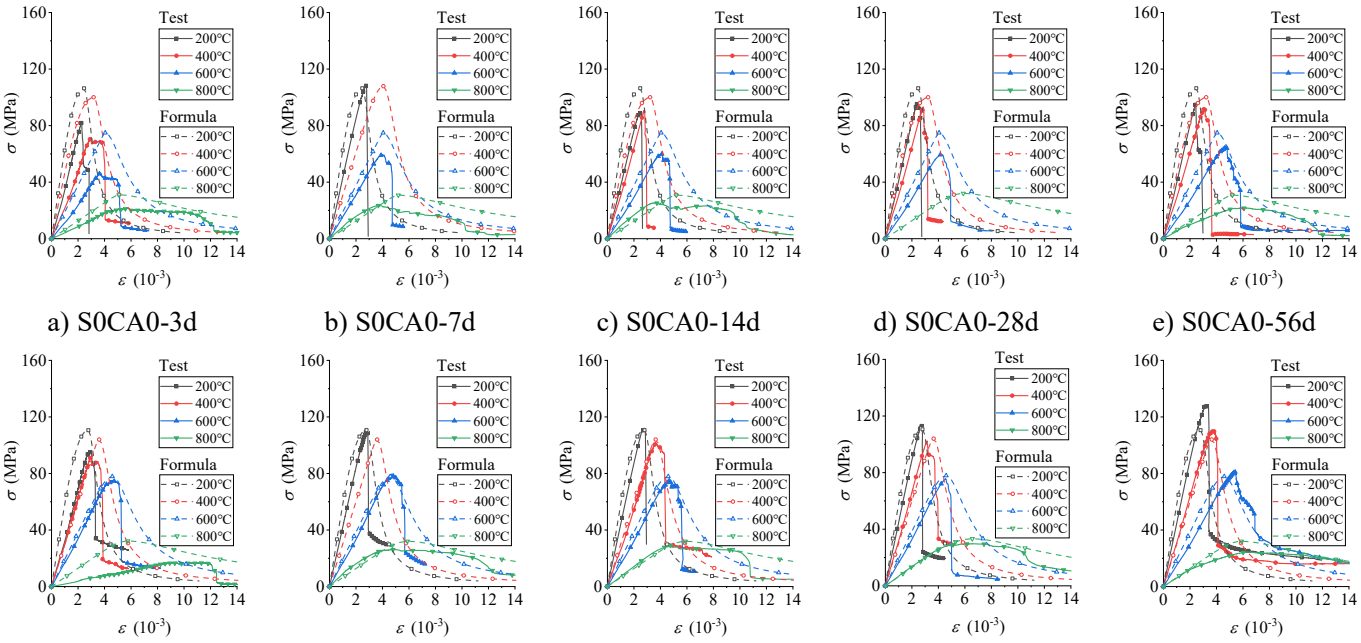


a) S0CA0-3d b) S0CA0-7d c) S0CA0-14d d) S0CA0-28d e) S0CA0-56d

f) S1CA0-3d g) S1CA0-7d h) S1CA0-14d i) S1CA0-28d j) S1CA0-56d

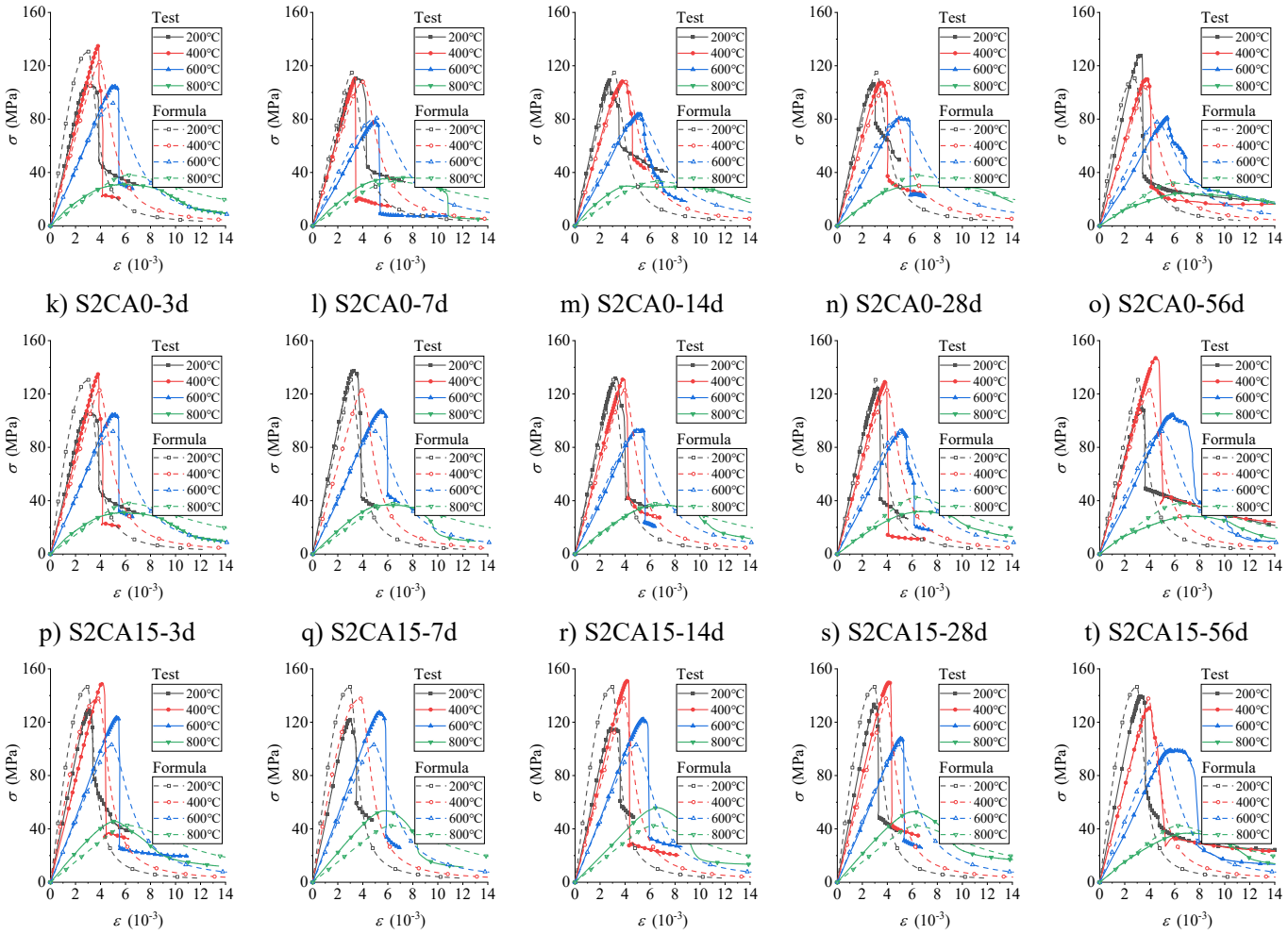


k) S2CA0-3d l) S2CA0-7d m) S2CA0-14d n) S2CA0-28d o) S2CA0-56d

p) S2CA15-3d q) S2CA15-7d r) S2CA15-14d s) S2CA15-28d t) S2CA15-56d

u) S2CA30-3d v) S2CA30-7d w) S2CA30-14d S2CA30-28d x) S2CA30-56d

Figure 17 The validation of the proposed stress-strain curve

To validate the proposed model, the stress-strain curves for the UHPC of different mixtures are generated using the current model and are plotted in Figure 17. The comparisons show that the proposed stress-strain model can accurately simulate the test results for the UHPC specimens exposed to elevated temperature at early age.

# 4 Microstructure analysis

The above investigation on the mechanical properties of the UHPC exposed to elevated temperature at different early age has shown distinctive residual performance at the early and hardened phases. This section aims to elucidate the degradation mechanisms under coupled influences of age and temperature, with a focus on the microstructural and phase compositions of the UHPC at differing ages after thermal exposure.

## 4.1 Scanning electron microscopy analysis

Figure 18 presents the SEM images of the UHPC paste exposed to elevated temperatures at various

ages. The images capture typical temperature levels of 400℃ and 800℃, representing general and extreme high temperature conditions, respectively, alongside observations at early (3 days) and matured (56 days) ages. The microstructure of the UHPC at ambient temperature is exceptionally dense, attributed to the very low water-to-binder ratio of 0.17 and the pozzolanic reaction between portlandite and silica fume. It can be found that after a 3-day exposure to 400℃, short rod-shaped ettringite (Aft) crystals are seen within the matrix, which typically decompose entirely below 200℃.This observation suggests that the UHPC undergoes a secondary hydration over a 56-day period at ambient temperature after the high temperature exposure, resulting in the formation of new hydration products. Additionally, a substantial amount of C-S-H remains present at this temperature. A part of the C-S-H results from the initial hydration process, while the others are formed through the secondary hydration as CH reacts with $SiO_2$ from silica fume during heating. A comparative analysis with the matured specimens at ambient conditions shows an increased porosity within the matrix under the stated thermal conditions. This increase suggests that while high temperatures facilitate hydration and pozzolanic reactions, the concurrent evaporation of water and dehydration decomposition of the hydration products contribute to pore coarsening and crack formation. At the macroscopic level, this manifests as sustained compressive strength albeit a reduced elastic modulus. Furthermore, the matrix of the post 56 days UHPC at 400℃ exhibits a denser structure compared to that after 3 days, indicating enhanced resistance to thermal degradation in the hardened phase of the UHPC. Consequently, the macroscopic properties such as compressive strength and elastic modulus of the UHPC demonstrate a progressive increase with the age at 400℃.

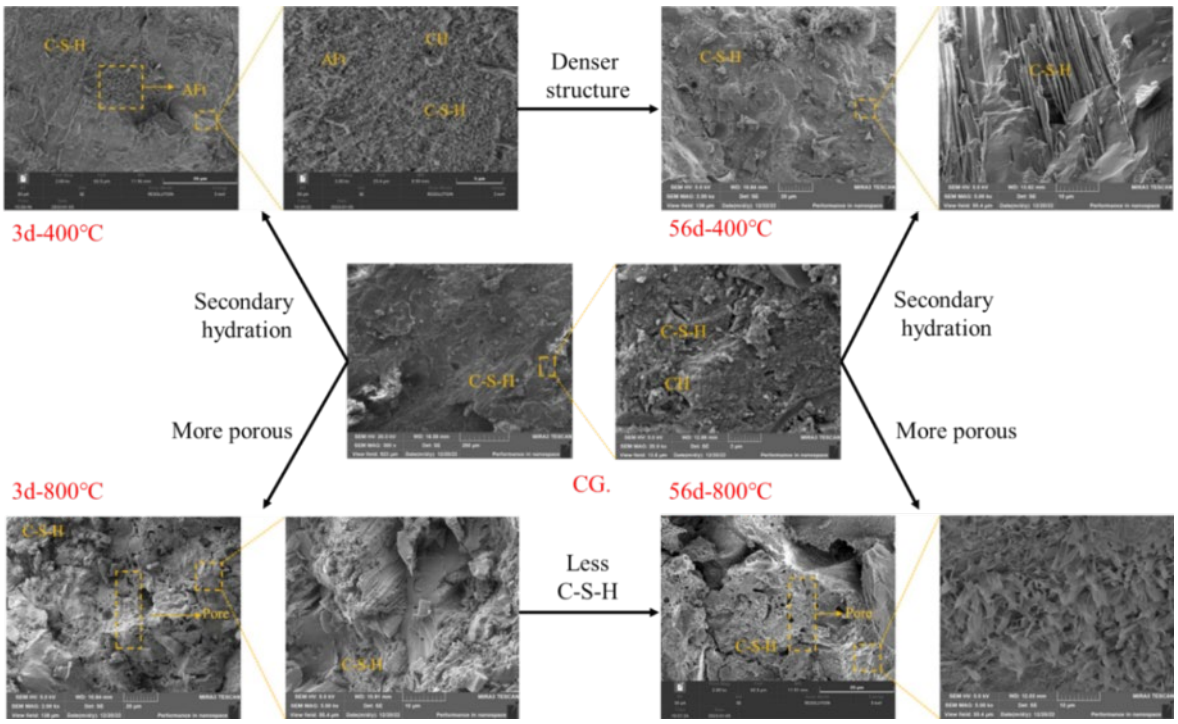


Figure 18 SEM images of UHPC paste exposed to elevated temperature at different early age

Figure 18 also presents the microstructure at 800℃, revealing substantial degradation of the UHPC structure. The material exhibits increased porosity and surface roughness, with a granular texture accompanied by numerous voids and microcracks. This deterioration is largely attributed to the decomposition of C-S-H phases. Moreover, the phase transformation of $SiO_2$ crystals induces volumetric expansion, while ongoing dehydration promotes volumetric contraction, resulting in uneven deformation and the formation of extensive cracking. These combined effects lead to a marked reduction in compressive strength and elastic modulus, as well as an increase in peak strain when compared to the UHPC maintained under ambient conditions.

At 800℃, CH is no longer detectable, although small quantities of C-S-H gel persist. This residual C-S-H likely originates from the rehydration of $C_nS$(Calcium silicate,e.g.$C_2S$,$C_3S$) and related compounds during the recuring phase. Specimens that underwent a 56-day initial curing exhibit even lower C-S-H content following 800℃ exposure, likely due to the shorter recuring duration, which restricts the extent of rehydration reactions.

### 4.2 X-Ray diffraction analysis

Figure 19 illustrates the XRD analysis of both the matured UHPC paste and the UHPC paste at varying ages following exposure to 400℃. The matured UHPC paste predominantly comprises chemical

constituents such as CH(Calcium hydroxide), $C_nS$(Calcium silicate), $SiO_2$(Silicon oxide), C-S-H(Calcium silicate hydrate), $Ca_2Al_2O_5$(Dicalcium aluminate), $CaCO_3$(Calcium carbonate), and CaO(Calcium oxide). Upon heating to 400℃, a noticeable reduction in CH and $SiO_2$ content is observed, accompanied by a significant increase in C-S-H. This transformation is attributed to the pozzolanic reaction induced at elevated temperatures, where CH and $SiO_2$ react to form additional C-S-H. The contents of $C_nS$, $CaCO_3$, and CaO, however, remain relatively unchanged. When comparing the hydration products of the UHPC paste at different ages after exposure to 400℃, it becomes apparent that the specimens with extended curing times have a higher C-S-H gel content. The formation of C-S-H gel arises mainly from two processes. The first process is natural hydration, in which the $C_nS$ phases in cement react with water to generate C-S-H gel. The second process occurs under high-temperature conditions, when CH reacts with $SiO_2$ from silica fume in a pozzolanic reaction, producing additional C-S-H gel. For the specimens with shorter curing durations, the C-S-H gel produced through natural hydration is relatively limited, while the pozzolanic reaction contributes a greater portion of the C-S-H gel. However, the total C-S-H content remains lower than in the specimens with longer curing times. Given the positive correlation between the C-S-H content and the mechanical strength of the paste, the compressive strength of the UHPC paste exposed to 400℃ increases with curing age. These findings align well with the experimental results discussed in Section 3, further validating the observed strength development under high-temperature conditions.

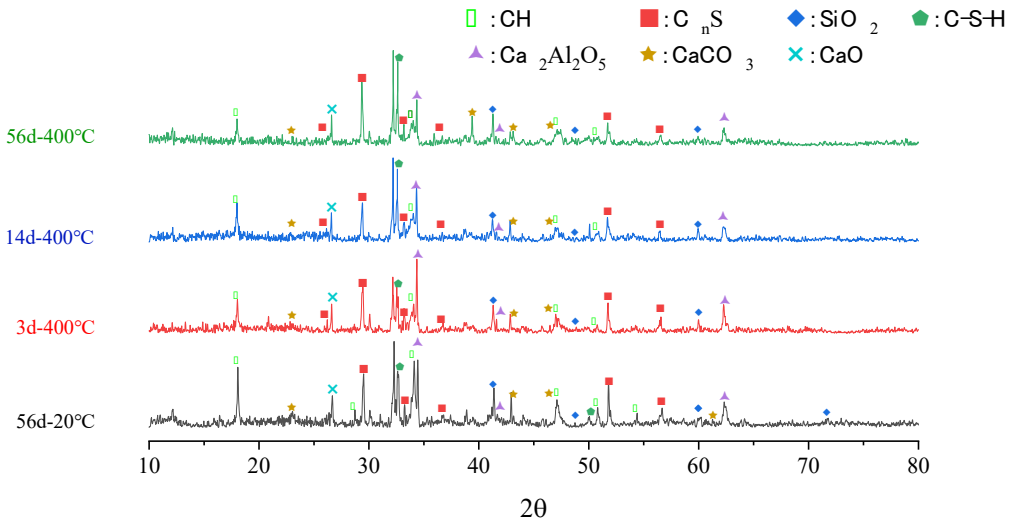


Figure 19 XRD graphs of UHPC paste exposed to 400 ℃

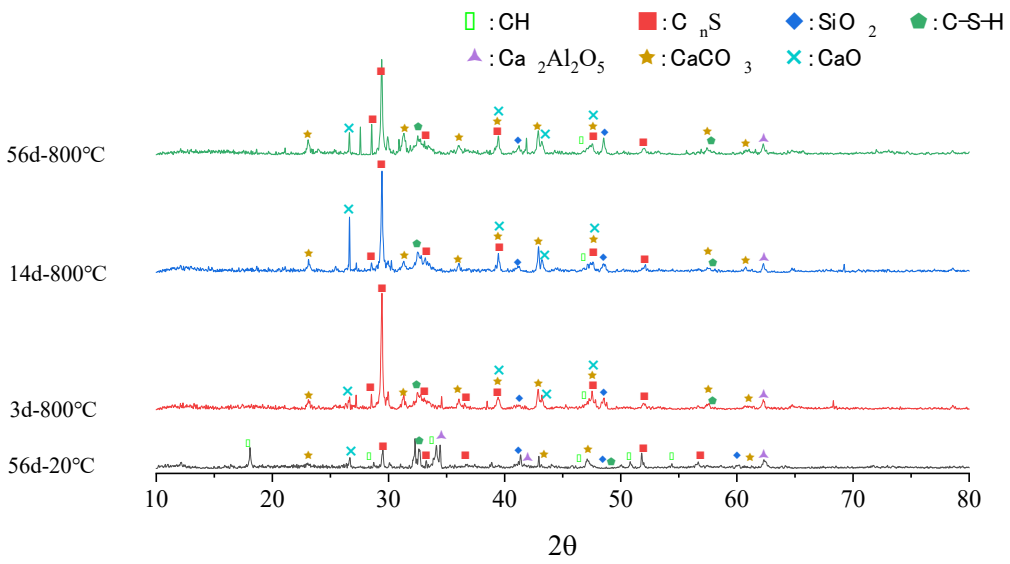


Figure 20 XRD graphs of UHPC paste exposed to 800 ℃

451

452 Figure 20 presents the XRD analysis results of both the matured UHPC paste and the UHPC paste at
453 different curing ages after exposure to 800℃. Compared to the matured UHPC paste, the specimens
454 subjected to 800℃ display a complete depletion of CH and an increase in both CaO and $CaCO_3$ contents.
455 This transformation occurs because CH decomposes into CaO within the 400~600℃ temperature range.
456 During the subsequent recuring process, the CaO undergoes carbonation, generating $CaCO_3$. Additionally,
457 a marked reduction in C-S-H content is observed, as the high-temperature environment leads to the
458 decomposition of C-S-H into $C_nS$. Although some $C_nS$ may rehydrate to form limited amounts of C-S-H
459 during recuring, the C-S-H content remains substantially lower than in the specimens cured at room
460 temperature, leading to a significant reduction in mechanical strength after exposure to 800℃.

461 Further comparison of the hydration products across the UHPC specimens of various curing ages
462 exposed to 800℃ reveals that the samples with extended initial curing exhibit notably lower levels of
463 $CaCO_3$ and C-S-H after high-temperature exposure. This reduction is due to the shorter recuring period
464 allowed for older specimens, which limits both the extent of carbonation and rehydration. Since $CaCO_3$ and
465 C-S-H positively correlate with material strength, the reduced formation of these compounds results in
466 lower residual strength in the specimens with longer curing ages after 800℃ exposure. These findings are
467 consistent with the macroscopic results discussed in Section 3, providing additional evidence for the impact
468 of high-temperature exposure on UHPC microstructure and strength retention.

### 4.3 MIP analysis

Figure 21 illustrates pore size distribution and porosity of the UHPC paste (S0CA0) at elevated temperatures and varying early ages. As temperature increases, pore coarsening is evident, with more larger pore and increased porosity. After exposure to 400° C, the porosity exceeds that observed at ambient conditions, suggesting a secondary hydration does not densify the structure. Samples aged 3 days exhibit greater porosity at 400°C than aged 56 days due to lower natural hydration, reflecting reduced resistance to thermal degradation of younger UHPC.

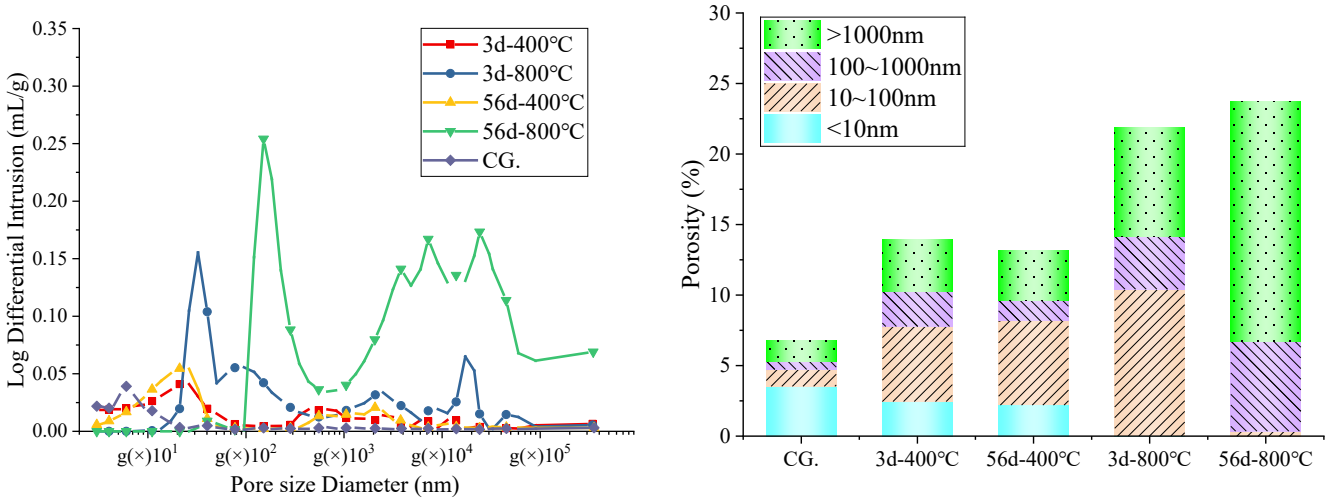


a) Pore size distribution b) Porosity

Figure 21 Pore distribution of UHPC paste (S0CA0) exposed to elevated temperature at different early age

At 800°C, there is a significant increase in the proportion of large pores and overall porosity due to the dehydration and decomposition of C-S-H and CH phases. Additionally, thermal cracking occurs from uneven expansion at high temperatures, further contributing to the coarsening of the pore structure. Comparing the porosity of the specimens exposed to 800°C after 3 and 56 days of curing, the porosity of the 3-day specimen is notably lower than that of the 56-day specimen. This can be attributed to the extended post-heating curing period for the 3-day specimen, during which CaO reacts with $CO_2$ in the air, forming $CaCO_3$. Additionally, the $C_nS$ phases undergo limited reaction with the moisture in the air to produce small amounts of C-S-H, resulting in a relatively lower porosity. These observations provide valuable insights into the microstructural changes in the UHPC at elevated temperatures, and the impacts on its mechanical performance and durability across different curing ages.

## 5 Conclusion

Uniaxial compressive tests were conducted to examine the mechanical responses of UHPC exposed

to elevated temperature at early age. The impacts of the age exposed to elevated temperature, temperature, steel fiber, and aggregate content on the failure modes, strength, modulus, peak strain, and stress-strain responses were studied. Microstructural characterization was performed using X-ray diffraction and scanning electron microscopy. An empirical model was developed to predict the post-fire mechanical properties of UHPC. The following conclusions can be drawn：

1) The failure morphology of the UHPC is mainly influenced by steel fiber content, coarse aggregate, and temperature, while concrete age has only minimal impact. A higher steel fiber content and coarse aggregates improve structural integrity and crack resistance, respectively. At 600°C and 800°C, a higher fiber content leads to more ductile failures, while a lower content results in brittle failures.
2) The residual compressive strength of the UHPC peaks around 400°C, increasing initially with temperature and then decreasing. The strength generally increases with age up to 600°C due to improved resistance and accelerated hydration. At 800°C, strength slightly decreases with age due to porosity and carbonation reactions. Adding steel fibers enhances strength and high-temperature resistance, while coarse aggregates increase crack formation due to inconsistent thermal deformation.
3) The elastic modulus of the UHPC decreases with the increase of temperatures due to the increased porosity. Age and steel fibers have little effect on elastic modulus, while coarse aggregates reduces degradation.
4) The peak strain of the UHPC increases with the increase of temperature due to porosity and cracking, except at 800°C where sintering reduces deformability. Early-age specimens exposed to high temperatures show higher carbonation and brittleness, resulting in lower peak strain compared to mature specimens.
5) When the temperature is below 600℃, the diffraction peaks of C-S-H gel increased with the increase of the age exposed to elevated temperature. At 800℃, the specimens of an earlier age exposed to elevated temperature have stronger diffraction peaks of C-S-H.

## Acknowledge

This study was supported financially by the National Natural Science Foundation of China (Grant NO.52178157).

## Reference

[1] R. Campbell, Fires in Structures Under Construction, in: NFPA, 2023. https://www.nfpa.org/education-and-

research/research/nfpa-research/fire-statistical-reports/fires-in-structures-under-construction.

[2] Fire breaks out in under-construction skyscraper in Hong Kong. https://efe.com/en/latest-news/2023-03-03/fire-breaks-out-in-under-construction-skyscraper-in-hong-kong/,2023.

[3] J. Franklin, DC Fire: Smoke in downtown DC coming from fire at high-rise under construction in Northwest,2021.https://www.wusa9.com/article/news/local/dc/dc-fire-smoke-from-fire-high-rise-under-construction-northwest/65-c2d7b5bc-23b6-491b-8f24-645be0519882.

[4] KOMO, 'It's devastating:' Massive fire destroys Everett waterfront apartments under construction, 2020. https://komonews.com/news/local/massive-fire-at-apartment-complex-under-construction-in-everett.

[5] D. Yoo, N. Banthia andY. Yoon, Recent development of innovative steel fibers for ultra-high-performance concrete (UHPC): A critical review, Cement Concr. Compos. 145(2024) 105359.

[6] J. Yang, B. Chen, J. Su, G. Xu, D. Zhang, J. Zhou, Effects of fibers on the mechanical properties of UHPC: A review, Journal of Traffic and Transportation Engineering (English Edition) 9(2022) 363-387.

[7] C. Kahanji, F. Ali, A. Nadjai, N. Alam, Effect of curing temperature on the behaviour of UHPFRC at elevated temperatures, Constr. Build. Mater. 182(2018) 670-681.

[8] J. Gong, G. Deng, B. Shan, Performance evaluation of RPC exposed to high temperature combining ultrasonic test: A case study, Constr. Build. Mater. 157(2017) 194-202

[9] W. Zheng, H. Li, Y. Wang, Compressive behaviour of hybrid fiber-reinforced reactive powder concrete after high temperature, Mater. Design. 41(2012) 403-409.

[10] J. Xiao, H. Falkner, On residual strength of high-performance concrete with and without polypropylene fibres at elevated temperatures, Fire. Safety. J. 41(2006) 115-121.

[11] M.M.S. Ridha, Combined effect of natural fibre and steel fibre on the thermal-mechanical properties of UHPC subjected to high temperature, Cement Concr. Res. 180(2024) 107510.

[12] X. Lyu, M. Elchalakani, T. Ahmed, M.A. Sadakkathulla, O. Youssf, Residual strength of steel fibre reinforced rubberised UHPC under elevated temperatures, J. Build. Eng. 76(2023) 107173.

[13] Y. Li, Y. Zhang, E. Yang, K.H. Tan, Effects of geometry and fraction of polypropylene fibers on permeability of ultra-high performance concrete after heat exposure, Cement Concr. Res. 116(2019) 168-178.

[14] C. Xue, M. Yu, H. Xu, L. Xu, M. Saafi, J. Ye, Compressive performance and deterioration mechanism of ultra-high performance concrete with coarse aggregates under and after heating, J. Build. Eng. 64(2023) 105502.

[15] L. Xu, Y. Yang, Y. Zhang, Y. Xue, Y. Yu, N. Hao, Estimation of stress-strain constitutive model for ultra-high

546 performance concrete after high temperature with an deep neural network based method, Constr. Build. Mater.
547 408(2023) 133690.
548 [16] J. Tang, W. Ma, Y. Pang, J. Fan, D. Liu, L. Zhao, S. Ahmed Sheikh, Uniaxial compression performance and
549 stress–strain constitutive model of the aluminate cement-based UHPC after high temperature, Constr. Build.
550 Mater. 309(2021) 125173.
551 [17] J. Park, Y. Kim, J. Cho, S. Jeon, Early-Age Strength of Ultra-High Performance Concrete in Various Curing
552 Conditions, Materials. 8(2015) 5537-5553.
553 [18] J. Camiletti, A.M. Soliman, M.L. Nehdi, Effects of nano- and micro-limestone addition on early-age properties
554 of ultra-high-performance concrete, Mater. Struct. 46(2013) 881-898.10.1617/s11527-012-9940-0
555 [19] Z. Mo, X. Gao, A. Su, Mechanical performances and microstructures of metakaolin contained UHPC matrix
556 under steam curing conditions, Constr. Build. Mater. 268(2021) 121112.
557 [20] S. Park, S. Wu, Z. Liu, S. Pyo, The Role of Supplementary Cementitious Materials (SCMs) in Ultra High
558 Performance Concrete (UHPC): A Review, Materials 14(2021) 1472.
559 [21] H. Wang , H. Lyu , T. Liu , et al. Effect of post-fire curing on compressive strength of ultra-high performance
560 concrete and mortar. Constr. Build. Mater. 346(2022)128447.
561 [22] Y. Li . Effect of post-fire curing and silica fume on permeability of ultra-high performance concrete. Constr. Build.
562 Mater. 290(2021)123175.
563 [23] Y. Qian , D. Yang , M. Liu , et al. Performance recovery of high-temperature damaged ultra-high-performance
564 concrete under different curing environments[J]. Dev. Built. Environ. 16(2023)100274.
565 [24] S. Dong, X. Ouyang, D. Yoo, et al. Influence of early thermal curing regimes on properties of ultra-high
566 performance concrete: A review. J. Build. Eng. 96(2024)110494.
567 [25] R. Nassar, O. Zaid , F. Althoey, et al. Spalling behavior and performance of ultra-high-performance concrete
568 subjected to elevated temperature: A review. Constr. Build. Mater. 2024,411:134489.
569 [26] T. Wang, M. Yu, X. Zhang, L. Xu, L. Huang, Experimental study and proposal of a design model of ultra-high
570 performance concrete filled steel tube columns subjected to fire, Eng. Struct. 280(2023) 115697.
571 [27] M. Yu, W. Liao, S. Liu, T. Wang, C. Yu, S. Cheng, Axial compressive performance of ultra-high performance
572 concrete-filled steel tube stub columns at different concrete age, Structures 55(2023) 664-676.
573 [28] T. Wang, M. Yu, X. Zhang, S. Cheng, S. Liu, Post-fire mechanical behaviour of ultra-high-performance
574 concrete-filled steel tube (UHPCFST) stub columns under compression, J. Constr. Steel. Res. 196(2022)

107384.

[29] T. Wang, M. Yu, X. Zhang, J. Ye, Experimental Study on Random Temperature Field of Ultra-High Performance Concrete Filled Steel Tube Columns under Elevated Temperature, Compos. Struct. 289(2022) 115445

[30] M. Reda, S. Chidiac. Performance of capsules in self-healing early-age concrete due to restrained shrinkage. Constr. Build. Mater.436( 2024)136984.

[31] Z. Zhao, K. Wang, D. Lange, et al. Creep and thermal cracking of ultra-high volume fly ash mass concrete at early age. Cem. Concr. Compos. 99( 2019)191-202.

[32] P. Mehta, N. Carino, H Jennings. Properties of concrete at early ages. Matériaux Et Construction. 13(2)(1980)265-274.

[33] G. Shi. Study on the Bearing Capacity of Early Age RC Columns after High Temperature-Recuring. China University of Mining and Technology Architectural and Civil Engineering. 2020.(In Chinese)

[34] Z. Liu, P. Van den Heede, C. Zhang, X. Shi, L. Wang, J. Li, Y. Yao, B. Lothenbach, N. De Belie, Carbonation of blast furnace slag concrete at different CO2 concentrations: Carbonation rate, phase assemblage, microstructure and thermodynamic modelling, Cement Concr. Res. 169(2023) 107161.

[35] G. Peng, X. Niu, Y. Shang, D. Zhang, X. Chen, H. Ding, Combined curing as a novel approach to improve resistance of ultra-high performance concrete to explosive spalling under high temperature and its mechanical properties, Cement Concr. Res. 109(2018) 147-158.

[36] L. Haiyan, W. Ying, X. Hengyan, Z. Wenzhong, Microstructure analysis of reactive poeder concrete after exposed to high temperature, J.Huazhong Univ.of Sci.&Tec.(Natural Science Edition) 40(2012) 71-75.(In Chinese)

[37] Y. Qian, D. Yang, Y. Xia, H. Gao, Z. Ma, Properties and improvement of ultra-high performance concrete with coarse aggregates and polypropylene fibers after high-temperature damage, Constr. Build. Mater. 364(2023) 129925.10.1016/j.conbuildmat.2022.129925

[38] M. Abid, X. Hou, W. Zheng and R. R. Hussain, High temperature and residual properties of reactive powder concrete-A review, Constr. Build. Mater. 147(2017) 339-351.

[39] S. Ahmad , R.A. Assaggaf , M. Maslehuddin , Effects of carbonation pressure and duration on strength evolution of concrete subjected to accelerated carbonation curing, Constr. Build. Mater. 136(2017)565-573.

[39] I. Netinger, D. Varevac, D. Bjegović, D. Morić, Effect of high temperature on properties of steel slag aggregate

concrete, Fire. Safety. J. 59(2013) 1-7.
[40] T. LV, G. ZHAO, L. Zhishen, Experimental study on mechanical properties of long standing concrete after exposure to high temperature, Journal of Building Structures 25(2004) 63-70.(In Chinese)
[41] C.K.H. Carreira D J, Stress-Strain Relationship for Plain Concrete in Compression, Journal of the American Concrete Institute 82(1985) 90362-90369.
[42] Z. Guo, Reinforced Concrete Theory and Analyse, in: Tsinghua University Press, 2003.(In Chinese)
[43] C.A.O.B. Sciences, Code for design of concrete structures, in: GB50010, China Architecture & Building Press, Beijing, 2010.(In Chinese)
[44] M. Yu, T. Wang, Y. Chi, D. Li, L. Li, F. Shi, Residual mechanical properties of GGBS-FA-SF blended geopolymer concrete after exposed to elevated temperatures, Constr. Build. Mater. 411(2024) 134378.
[45] T. Wang, M. Yu, H. Lin, D. Li, L. Li, Experimental investigation of mechanical properties of GGBS-FA-SF blended geopolymer concrete at elevated temperatures, Fire. Safety. J. 146(2024) 104156.
[46] T. Wang, M. Yu, W. Shan, L. Xu, S. Cheng, L. Li, Post-fire compressive stress–strain behaviour of steel fibre reinforced recycled aggregate concrete, Compos. Struct. 309(2023) 116735.